CrossMark

J. Fluid Mech. (2019), *vol.* 874, *pp.* 5–37. © Cambridge University Press 2019
doi:10.1017/jfm.2019.451

Effect of finite conductivity on the nonlinear behaviour of an electrically charged viscoelastic liquid jet

Fang Li[1,†], Shi-You Ke[1], Xie-Yuan Yin[1] and Xie-Zhen Yin[1]

[1]Department of Modern Mechanics, University of Science and Technology of China, Hefei, Anhui 230027, PR China

(Received 19 December 2018; revised 30 May 2019; accepted 31 May 2019; first published online 3 July 2019)

In this paper a one-dimensional numerical study on the nonlinear behaviour of an electrically charged jet of Oldroyd-B viscoelastic, Taylor–Melcher leaky dielectric liquid is carried out. The effect of surface charge level, axial wavenumber and finite conductivity on the nonlinear evolution of the jet is investigated. Different structures including beads-on-a-string with/without satellite droplets, quasi-spikes and spikes are detected, and their domains in the plane of the non-dimensional axial wavenumber and the electrical Bond number are illustrated. The underlying mechanisms in the formation of the structures are examined. It is found that tangential electrostatic force plays a key role in the formation of a quasi-spike structure. Decreasing liquid conductivity may lead to a decrease in the size of satellite droplets or even the complete removal of them from a beads-on-a-string structure, induce the transition from a beads-on-a-string to a quasi-spike structure or postpone the appearance of a spike. On the other hand, finite conductivity has little influence on filament thinning in a beads-on-a-string structure, owing to the fact that the electrostatic forces are of secondary importance compared with the capillary force. The difference between the finite conductivity, large conductivity and other cases is elucidated. An experiment is carried out to observe spike structures.

Key words: jets, nonlinear instability, viscoelasticity

1. Introduction

1.1. *Nonlinear dynamics of viscoelastic liquid jets*

Non-Newtonian viscoelastic liquid jets are often encountered in applications such as inkjet printing, fuel atomization, micro/nano-fibre manufacture, industrial prilling, microfluidics, pharmaceuticals and rheological measurements (Eggers & Villermaux 2008; Zell *et al.* 2010; Basaran, Gao & Bhat 2013; Alsharif, Uddin & Afzaal 2015). The study of the instability and break-up of viscoelastic jets is of both theoretical and practical interest. Upon a small axisymmetric disturbance being imposed, a jet is perturbed and starts to deform. It has been well recognized that the growth of the disturbance at initial times can be predicted by linear theory (Rayleigh 1878, 1879).

† Email address for correspondence: fli6@ustc.edu.cn

https://doi.org/10.1017/jfm.2019.451 Published online by Cambridge University Press

However, as the deformation of the jet grows, a nonlinear effect comes into play. Particularly for a viscoelastic jet, due to viscoelasticity, break-up can be greatly postponed: the jet experiences a slow necking process and evolves into a quasistatic beads-on-a-string structure with large primary droplets connected by a thin filament, sometimes accompanied by small secondary droplets between the primary ones (Bousfield *et al.* 1986; Entov & Hinch 1997; Chang, Demekhin & Kalaidin 1999; Anna & McKinley 2001; Christanti & Walker 2001, 2002; Clasen *et al.* 2006; Oliveira, Yeh & McKinley 2006; Malkin, Arinstein & Kulichikhin 2014; Wagner, Bourouiba & McKinley 2015; Deblais, Velikov & Bonn 2018).

To date the nonlinear behaviour of viscoelastic jets has been extensively studied theoretically, numerically and experimentally. To facilitate the theoretical and numerical aspects, many researchers employed one-dimensional (1-D) viscoelastic models based on the slender body approximation (Bousfield *et al.* 1986; Schümmer & Thelen 1988; Chang *et al.* 1999; Li & Fontelos 2003; Clasen *et al.* 2006; Ardekani, Sharma & McKinley 2010; Bhat *et al.* 2010, 2012). The validity of these 1-D viscous or viscoelastic models has been examined and justified by comparing with the two-dimensional (2-D) algorithms and experimental results (Ambravaneswaran, Wilkes & Basaran 2002; López-Herrera & Gañán-Calvo 2004; Wagner *et al.* 2005; Collins, Harris & Basaran 2007; Eggers & Villermaux 2008; Tembely *et al.* 2012; Turkoz *et al.* 2018). In the 1-D analyses, the most significant finding is the scaling laws followed by the thinning of the filament for a viscoelastic jet of Oldroyd-B type. That is, the thickness of the filament decreases exponentially with time at a rate of $1/3De$ (De is the Deborah number defined as the ratio of the stress relaxation time to the capillary time), whereas the polymeric stress inside the filament increases exponentially with time at the same rate (Chang *et al.* 1999; Clasen *et al.* 2006). Besides, the self-similarity in the corner region joining the droplet to the filament was explored theoretically with the aid of 1-D models (Clasen *et al.* 2006; Bhat *et al.* 2012). The dynamics of droplets in highly stretched viscoelastic jets was investigated by Li & Fontelos (2003). The formation of satellite droplets in beads-on-a-string structures as well as the way to eliminate them was explored by Ardekani *et al.* (2010) and Bhat *et al.* (2010). Beyond Oldroyd-B liquids, other types such as upper-convected Jeffreys, Giesekus and FENE-P fluids were also examined (Schümmer & Thelen 1988; Fontelos & Li 2004; Ardekani *et al.* 2010).

In addition to the 1-D studies, a few direct numerical simulations have been carried out. Morrison & Harlen (2010) used a Lagrangian–Eulerian finite-element method to simulate the deformation and break-up of FENE-CR viscoelastic liquid flows ejected from a nozzle in the drop-on-demand inkjet printing process. Gupta & Chokshi (2015) conducted a weakly nonlinear stability analysis of the extensional flow of an extended Pom-Pom polymer jet perturbed by a finite-amplitude disturbance. Using the volume-of-fluid method to track the interface and the log-conformation transformation to solve the constitutive equation, Turkoz *et al.* (2018) performed a direct numerical simulation of the axisymmetric thinning of a viscoelastic filament of Oldroyd-B liquid. Their 2-D simulations provided some details of the velocity and the stresses in the entire thread.

The relevant experimental investigation is much more prosperous. A great number of experiments have been dedicated to the capillary thinning and break-up of viscoelastic liquid jets (Tirtaatmadja, McKinley & Cooper-White 2006; Bazilevskii & Rozhkov 2014; Kulichikhin *et al.* 2014; Malkin *et al.* 2014; Greiciunas *et al.* 2017; Jimenez *et al.* 2018; Mathues *et al.* 2018; Varchanis *et al.* 2018). These experimental studies elucidated the nonlinear pinch-off dynamics of viscoelastic jets, the formation of primary and satellite droplets, the extensional rheological properties of viscoelastic

https://doi.org/10.1017/jfm.2019.451 Published online by Cambridge University Press

liquids, the effect of the molecular weight and concentration of the polymer, the phase separation phenomenon, as well as the feasibility and productivity of extensional flows in distinct applications such as inkjet printing, fibre spinning, rheometers and blood plasma. Among them, Wagner *et al.* (2005) found that the addition of a small amount of polymer may significantly delay the detachment of a water drop and lead to the formation of a long-lived filament with secondary beads on it in certain conditions. Clasen *et al.* (2009) explored the mechanism in the transition from dripping to jetting and found that the viscoelastic filament exerts an axial tensile force on the adjacent drops, which, together with the capillary, inertial and gravitational forces, controls the detachment of the terminal drop. Sattler, Wagner & Eggers (2008), Sattler *et al.* (2012), Kulichikhin *et al.* (2014), and Eggers (2014) studied the blistering pattern with different generations of small droplets on the filament as well as the instability and phase separation in it.

1.2. *Nonlinear dynamics of electrified liquid jets*

In electrospraying and electrospinning experiments, the electric field has been shown to be a novel, easy way to control the linear and nonlinear behaviour of liquid jets (Yu, Fridrikh & Rutledge 2006; Eda & Shivkumar 2007; Ismail *et al.* 2016; Wang, Wang & Hashimoto 2016; Wang *et al.* 2018). The coupling of the electric field with the flow field gives rise to new phenomena of instability and rupture of jets, and exploring the underlying mechanisms undoubtedly enriches the fundamentals in electrokinetics and electrohydrodynamics. On the other hand, owing to simplicity, efficiency and flexibility in producing monodisperse droplets and ultra-thin fibres at micro/nanometre scales, electrified jets are very popular in various applications involving electrohydrodynamic, electrochemical or biomechanical processes. The relevant experimental studies are too numerous to mention. To gain a comprehensive understanding of those fundamentals in physics and the latest progress in diverse applications, the interested readers are referred to several recent reviews contributed by Onses *et al.* (2015), Gañán-Calvo *et al.* (2018), Rosell-Llompart, Grifoll & Loscertales (2018) and Yoon *et al.* (2018).

Due to the complexity of the problem, only a few theoretical and numerical reports have addressed the nonlinear axisymmetric instability of electrified jets in the literature. As in the study of viscoelastic jets, 1-D models were used to facilitate theoretical analysis and save computational time (López-Herrera, Gañán-Calvo & Perez-Saborid 1999; Feng 2003; Elcoot 2007; Wang, Mählmann & Papageorgiou 2009; Li, Yin & Yin 2016, 2017*b*). Among them, López-Herrera *et al.* (1999) developed a 1-D model to investigate the nonlinear deformation and break-up of an electrically charged viscous liquid jet of infinite conductivity. Feng (2003) studied the stretching of a straight electrically charged viscoelastic jet of Giesekus liquid. Wang *et al.* (2009) simulated the axisymmetric nonlinear dynamics of a perfectly conducting, viscous liquid jet under the action of a radial electric field. Li *et al.* (2016) built a 1-D model to study the nonlinear behaviour of a perfectly conducting, slightly viscoelastic liquid jet under a radial electric field. Later, they investigated the transition from beads-on-a-string to spike structure under a sufficiently large electric field (Li *et al.* 2017*b*). As in a viscous flow (Wang *et al.* 2009), the singular spike structure arising in a viscoelastic jet was found to possess a self-similar characteristic.

Some direct numerical simulations have been performed (Setiawan & Heister 1997; Higuera 2003, 2006; Collins *et al.* 2007; Wang & Papageorgiou 2011; Wang 2012; López-Herrera *et al.* 2015; Lakdawala, Sharma & Thaokar 2016). Setiawan & Heister (1997) utilized the boundary element method to calculate the time-dependent

https://doi.org/10.1017/jfm.2019.451 Published online by Cambridge University Press

evolution of a perfectly conducting, inviscid liquid jet subjected to a radial electric field. Higuera (2003, 2006) numerically simulated the cone-to-jet structure of a conducting viscous liquid jet in electrospraying. Collins *et al.* (2007) developed a robust Galerkin finite-element algorithm to solve the 2-D Navier–Stokes equation and Laplace equation governing the axisymmetric deformation and break-up of a perfectly conducting, incompressible Newtonian liquid jet under a radial electric field. With the aid of the boundary integral method, Wang & Papageorgiou (2011) studied the axisymmetric break-up of a perfectly conducting, viscous liquid thread immersed in another non-conducting, viscous liquid, in the limit of zero Reynolds number. Later, Wang (2012) extended this study to the poorly conducting case. Using a volume-of-fluid method, López-Herrera *et al.* (2015) simulated the break-up of an electrically charged liquid jet at time scales comparable to or smaller than the diffusion and electroosmotic migration times. Lakdawala *et al.* (2016) presented a dual grid level set method (DGLSM) to numerically study the nonlinear break-up dynamics of a perfectly conducting, Newtonian viscous liquid jet under a radial electric field.

1.3. *The present work*

In the present work we incorporate the Oldroyd-B viscoelastic model with the Taylor–Melcher leaky dielectric theory and elaborate on the nonlinear dynamics of an electrically charged viscoelastic liquid jet of finite conductivity. The Oldroyd-B model, which requires constant viscosity and high elasticity of the liquid, is the simplest nonlinear viscoelastic model suitable to describe large deformations of dilute polymer solutions (Prilutski *et al.* 1983; James 2009). It has been successfully used to investigate the asymptotic behaviour, scaling laws and self-similar characteristic at the late stages of capillary thinning of viscoelastic liquid jets (Chang *et al.* 1999; Clasen *et al.* 2006; Ardekani *et al.* 2010; Bhat *et al.* 2010; Turkoz *et al.* 2018). The disadvantage of the model is that it cannot describe the final pinch-off of a viscoelastic jet, for its hypothesis of infinite extensibility of macromolecular chains. To study the pinch-off of viscoelastic jets, a more complicated constitutive equation that allows finite extensibility should be used, such as the Giesekus or FENE-P model. Nevertheless, for primary research on the deformation process of an electrified viscoelastic jet from the initial to large times, the Oldroyd-B model is appropriate. In electrohydrodynamics, the Taylor–Melcher leaky dielectric theory has been widely used to formulate flows of poorly conducting liquids. It consists of the Navier–Stokes equation describing fluid motion, an expression for the conservation of bulk electric current, an equation describing the conservation of surface charge, the Gauss law and the balance of forces on a fluid–fluid interface (Melcher & Taylor 1969; Saville 1997; Gañán-Calvo *et al.* 2018). The theory states that there is no charge in the fluid bulk. All charges are located on the interface between the fluids, and only on the interface does the electric field couple with the flow field. Different from a perfect conductor, for which the electrical force is perpendicular to the interface, a leaky dielectric permits the existence of a tangential electric field and tangential electrical force on the interface, which may influence the fluid motion significantly.

The paper is organized as follows. In § 2, the 1-D model is presented. In § 3, the equations and boundary conditions are solved numerically by means of a hybrid algorithm; different nonlinear structures are identified, the mechanisms in the formation of the structures are elucidated and the domains in the plane of the axial wavenumber and the electrical Bond number are delineated; the effect of

https://doi.org/10.1017/jfm.2019.451 Published online by Cambridge University Press

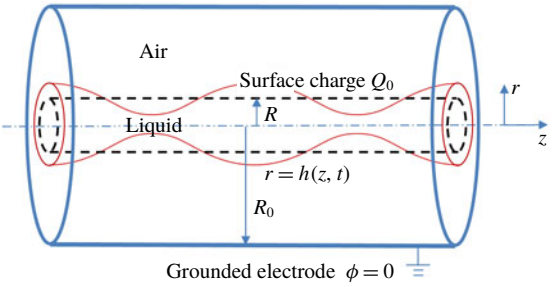

FIGURE 1. (Colour online) Schematic of the theoretical model.

finite conductivity on the beads-on-a-string and the spike structures is illustrated; the difference between the finite conductivity and large conductivity cases is discussed. In § 4, an experimental observation of the spike structure is presented. In § 5, the main conclusion is drawn.

2. One-dimensional model

Consider an infinitely long cylindrical liquid jet of radius R and velocity U surrounded by quiescent atmospheric air, as sketched in figure 1. For mathematical convenience, a relative cylindrical coordinate system (r, θ, z) moving together with the jet is used to formulate the problem, where r, θ and z are the radial, azimuthal and axial coordinates, respectively. The hydrodynamic effect of the air, as well as the effect of the gravitational force, temperature, mass transfer and magnetic field, is neglected. In practical applications such as inkjet printing, electrospraying and electrospinning, a viscoelastic liquid jet emitted from a capillary tube or the tip of a Taylor cone is inevitably accompanied by unrelaxed elastic stresses. The unrelaxed stresses have been shown to play a significant role in the instability and nonlinear behaviour of viscoelastic jets (Ruo *et al.* 2012; Mohamed *et al.* 2015; Mathues *et al.* 2018). Nevertheless, in the present study, we focus on the effect of finite conductivity on the nonlinear evolution of charged viscoelastic jets, and simply assume that there is no unrelaxed elastic stress in the base flow.

The liquid is assumed to be a dilute polymer solution of Oldroyd-B type. For an Oldroyd-B viscoelastic liquid, the deviatoric stress $\boldsymbol{\tau}$ can be decomposed into two parts, i.e. $\boldsymbol{\tau} = \boldsymbol{\tau}_s + \boldsymbol{\tau}_p$, where $\boldsymbol{\tau}_s$ and $\boldsymbol{\tau}_p$ are the contributions from the solvent and the polymer to the stress, respectively (James 2009). The constitutive equation for the solvent stress $\boldsymbol{\tau}_s$ is

$$\boldsymbol{\tau}_s = 2\eta_s \boldsymbol{D}, \tag{2.1}$$

where η_s is the solvent viscosity, and $\boldsymbol{D} = 1/2(\nabla \boldsymbol{v} + (\nabla \boldsymbol{v})^{\mathrm{T}})$ with $\boldsymbol{v}$ the velocity vector and superscript T denoting transpose is the rate-of-strain tensor. The constitutive equation for the polymeric stress $\boldsymbol{\tau}_p$ is

$$\boldsymbol{\tau}_p + \lambda_1 \widehat{\boldsymbol{\tau}}_p = 2\eta_p \boldsymbol{D}, \tag{2.2}$$

where λ_1 is the stress relaxation time, η_p is the polymeric viscosity and the hat denotes the upper convected time derivative,

$$\widehat{\boldsymbol{\tau}}_p = \frac{\partial \boldsymbol{\tau}_p}{\partial t} + (\boldsymbol{v} \cdot \nabla)\boldsymbol{\tau}_p - (\nabla \boldsymbol{v})^{\mathrm{T}} \cdot \boldsymbol{\tau}_p - \boldsymbol{\tau}_p \cdot \nabla \boldsymbol{v}. \tag{2.3}$$

https://doi.org/10.1017/jfm.2019.451 Published online by Cambridge University Press

On the other hand, the liquid is assumed to be a poor conductor of finite electrical conductivity K and electrical permittivity ε. The electrical relaxation time of the liquid, $t_e = \varepsilon/K$, is supposed to be comparable to or larger than the characteristic hydrodynamic time, say, the capillary time $t_c = \sqrt{\rho R^3/\sigma}$ with ρ the density of the liquid and σ the surface tension coefficient. At the initial time, free charges of density Q_0 are imposed uniformly on the surface of the jet. Meanwhile, a grounded annular electrode is positioned coaxially surrounding the jet at $r = R_0$. Considering that the air is a dielectric of negligible electrical conductivity, a basic radial electric field of strength $Q_0 R/\varepsilon_a r$, where ε_a is the electrical permittivity of the air, is sustained in the air phase. The entire jet is equipotential. Once the jet is perturbed, it begins to deform. Due to its large electrical relaxation time, charges cannot be redistributed in time on the surface, and the jet becomes non-equipotential. In such a case, the Taylor–Melcher leaky dielectric theory applies, in which the motion of the charges is governed by the following conservation equation (Melcher & Taylor 1969; Saville 1997),

$$\frac{\partial q}{\partial t} + \nabla_s \cdot (q\boldsymbol{v}) - K\boldsymbol{E}\cdot\boldsymbol{n} = 0, \tag{2.4}$$

where q is the surface charge density, $\nabla_s = (\boldsymbol{I} - \boldsymbol{nn})\cdot\nabla$ with $\boldsymbol{I}$ the unit tensor is the surface gradient, $\boldsymbol{n}$ the outward unit vector normal to the surface and $\boldsymbol{E}$ the electric field strength in the liquid phase.

The equations governing the flow field are the continuity and the momentum equations for incompressible flow, i.e.

$$\nabla\cdot\boldsymbol{v} = 0, \tag{2.5}$$

$$\rho\left(\frac{\partial \boldsymbol{v}}{\partial t} + \boldsymbol{v}\cdot\nabla\boldsymbol{v}\right) = -\nabla p + \nabla\cdot\boldsymbol{\tau}, \tag{2.6}$$

where p is the pressure.

Since the electric field is irrotational, an electrical potential function ϕ can be introduced. Due to the absence of bulk charge, ϕ satisfies the Laplace equation,

$$\nabla^2\phi_{,a} = 0, \tag{2.7}$$

where subscript a represents the air phase and no subscript represents the liquid phase. The electric field strength $\boldsymbol{E}_{,a} = -\nabla\phi_{,a}$.

At the grounded electrode $r = R_0$, the electrical potential is maintained at zero, i.e.

$$\phi_a(r = R_0, z, t) = 0. \tag{2.8}$$

The boundary conditions at the perturbed jet surface, $r = h(z, t)$, include the kinematic condition

$$v = \left(\frac{\partial}{\partial t} + \boldsymbol{v}\cdot\nabla\right)h, \tag{2.9}$$

where v is the velocity component in the radial direction, the dynamic condition

$$(\boldsymbol{T}_a^e - \boldsymbol{T}^h - \boldsymbol{T}^e)\cdot\boldsymbol{n} = \sigma\nabla\cdot\boldsymbol{nn}, \tag{2.10}$$

https://doi.org/10.1017/jfm.2019.451 Published online by Cambridge University Press

where $\boldsymbol{T}^h = -p\boldsymbol{I} + \boldsymbol{\tau}$ is the hydrodynamic stress, $\boldsymbol{T}^e = \varepsilon \boldsymbol{E}\boldsymbol{E} - (\varepsilon/2)\boldsymbol{E}\cdot\boldsymbol{E}\boldsymbol{I}$ is the electrical Maxwell stress, and $\boldsymbol{\nabla}\cdot\boldsymbol{n}$ is twice the local mean curvature, the continuity of the tangential electric fields,

$$\boldsymbol{n}\times(\boldsymbol{E}_a - \boldsymbol{E}) = 0, \tag{2.11}$$

and the Gauss law,

$$\boldsymbol{n}\cdot(\varepsilon_a \boldsymbol{E}_a - \varepsilon\boldsymbol{E}) = q. \tag{2.12}$$

An equivalent condition of (2.11) is the continuity of the electrical potentials across the air–liquid interface, i.e.

$$\phi_a(r=h, z, t) = \phi(r=h, z, t). \tag{2.13}$$

If the variation of the radius of the jet along the axial direction is gradual, the jet can be regarded as a slender body and a 1-D analysis can be implemented. Under the slender body approximation, the governing equations (2.5) and (2.6) together with the constitutive equations (2.1)–(2.3) and the boundary conditions (2.4), (2.9)–(2.12) yield

$$\frac{\partial h}{\partial t} + u\frac{\partial h}{\partial z} = -\frac{h}{2}\frac{\partial u}{\partial z}, \tag{2.14}$$

$$\begin{aligned}\frac{\partial u}{\partial t} + u\frac{\partial u}{\partial z} &= \chi\frac{\partial}{\partial z}\left[(E_{an}^2 - E_t^2) - \varepsilon_r(E_n^2 - E_t^2)\right] + \frac{4\chi E_t q}{h}\left[1+\left(\frac{\partial h}{\partial z}\right)^2\right] \\ &\quad - \frac{\partial(\boldsymbol{\nabla}\cdot\boldsymbol{n})}{\partial z} + 3\beta Oh\frac{1}{h^2}\frac{\partial}{\partial z}(h^2\frac{\partial u}{\partial z}) + \frac{1}{h^2}\frac{\partial}{\partial z}[h^2(\tau_{zz}-\tau_{rr})],\end{aligned} \tag{2.15}$$

$$\boldsymbol{\nabla}\cdot\boldsymbol{n} = \frac{1}{\left[1+\left(\dfrac{\partial h}{\partial z}\right)^2\right]^{3/2}}\left[\frac{1+\left(\dfrac{\partial h}{\partial z}\right)^2}{h} - \frac{\partial^2 h}{\partial z^2}\right], \tag{2.16}$$

$$\tau_{zz} + De\left(\frac{\partial \tau_{zz}}{\partial t} + u\frac{\partial \tau_{zz}}{\partial z} - 2\tau_{zz}\frac{\partial u}{\partial z}\right) = 2(1-\beta)Oh\frac{\partial u}{\partial z}, \tag{2.17}$$

$$\tau_{rr} + De\left(\frac{\partial \tau_{rr}}{\partial t} + u\frac{\partial \tau_{rr}}{\partial z} + \tau_{rr}\frac{\partial u}{\partial z}\right) = -(1-\beta)Oh\frac{\partial u}{\partial z}, \tag{2.18}$$

$$\frac{\partial q}{\partial t} + u\frac{\partial q}{\partial z} + \frac{q}{2}\frac{\partial u}{\partial z} - \tau\varepsilon_r E_n = 0, \tag{2.19}$$

where u is the velocity component in the axial direction, E_n and E_t are the normal and tangential electric fields, respectively, and τ_{zz} and τ_{rr} are the $zz-$ and $rr-$ components of the polymeric stress $\boldsymbol{\tau}_p$, respectively. Note that the 1-D equations (2.14)–(2.19) are non-dimensionalized by choosing the radius of the jet R, the capillary time t_c, the zero-shear viscosity $\eta_0 = \eta_s + \eta_p$, the capillary force σ/R, the electric field strength at the jet surface Q_0/ε_a and the electrical permittivity of the air ε_a as scales of length, time, viscosity, pressure, electric field and electrical permittivity, respectively. For the sake of simplicity, the same symbols are used in the equations to denote the corresponding dimensionless quantities. The derivation process of the above 1-D equations can be found in appendix A. The non-dimensional parameters involved are

https://doi.org/10.1017/jfm.2019.451 Published online by Cambridge University Press

(i) the Ohnesorge number $Oh = \eta_0/\sqrt{\rho\sigma R}$ representing the relative importance of viscosity and capillarity;
(ii) the Deborah number $De = \lambda_1/t_c$ representing the relative importance of elasticity and capillarity;
(iii) the solvent to solution viscosity ratio $\beta = \eta_s/\eta_0$;
(iv) the electrical Bond number $\chi = Q_0^2 R/2\varepsilon_a\sigma$ measuring the ratio of the electrostatic to the capillary force;
(v) the relative electrical permittivity $\varepsilon_r = \varepsilon/\varepsilon_a$;
(vi) the relative electrical relaxation time $\tau = t_c/t_e$.

In this 1-D system, equations (2.14) and (2.15) express the conservation of mass and momentum, respectively; equation (2.16) is the full expression of the curvature; equations (2.17) and (2.18) are the constitutive equations of the polymeric stress components τ_{zz} and τ_{rr}, respectively; equation (2.19) expresses the conservation of surface charge. To facilitate the calculation, the long wave approximation was applied to the electric field in Wang (2012). Upon doing so, only two terms related to the electric field, i.e. χq^2 (a simplified electrostatic pressure) and $-4\chi(q/h)(\partial\phi/\partial z)$ (a simplified tangential electrostatic force), remain in the momentum equation. However, this simplification might lead to significant inaccuracy, since the electrostatic forces are important factors influencing the flow. In order to make the 1-D simulation more accurate, we choose not to simplify the electric field, as performed in López-Herrera *et al.* (1999) and Collins *et al.* (2007).

Different from the 1-D models for perfectly conducting liquid jets in which only one term related to the electric field, i.e. the electrostatic pressure originating from the normal electric field in the air phase, $-\chi E_{an}^2$, appears in the momentum equation (Setiawan & Heister 1997; López-Herrera *et al.* 1999; Li *et al.* 2016), here in the leaky dielectric case, besides E_{an}, both the normal electric field in the liquid phase E_n and the tangential electric field E_t exist, which contribute to the electrostatic pressure. Moreover, the existence of surface charge and tangential electric field gives rise to a tangential electrostatic force on the jet surface, which plays a role in the balance of the forces. The simplicity of the 1-D models for perfectly conducting liquid jets also lies in the fact that the surface conservation (2.19) is absent (Setiawan & Heister 1997; López-Herrera *et al.* 1999; Li *et al.* 2016).

Also note that an alternative form of the momentum equation (2.15) is

$$\frac{\mathrm{d}u}{\mathrm{d}t} = -\frac{\partial(p_\sigma + p_e)}{\partial z} + f_{et} + \frac{1}{h^2}\frac{\partial}{\partial z}\left[h^2\left(3\beta Oh\frac{\partial u}{\partial z} + \Phi\right)\right], \tag{2.20}$$

where $\mathrm{d}u/\mathrm{d}t$ is the material derivative of the axial velocity u of a fluid element, and the terms on the right-hand side are the factors (the capillary, electrical, viscous and elastic forces) influencing the motion of the fluid element. Among them, $p_\sigma = \boldsymbol{\nabla}\cdot\boldsymbol{n}$ is the capillary pressure, $p_e = -\chi[(E_{an}^2 - E_t^2) - \varepsilon_r(E_n^2 - E_t^2)]$ is the jump in electrostatic pressure across the jet surface (hereafter this is called the electrostatic pressure for brevity), $f_{et} = 4\chi E_t q h^{-1}[1 + (\partial h/\partial z)^2]$ is the tangential electrostatic force and $\Phi = \tau_{zz} - \tau_{rr}$ is the first normal stress difference.

At the initial time $t = 0$, a small harmonic disturbance is imposed on the surface of the jet, i.e.

$$h(z, t = 0) = \sqrt{1 - \frac{\varepsilon_0^2}{2}} + \varepsilon_0\cos(kz), \tag{2.21}$$

https://doi.org/10.1017/jfm.2019.451 Published online by Cambridge University Press

$$u(z, t=0) = \tau_{zz}(z, t=0) = \tau_{rr}(z, t=0) = 0, \tag{2.22}$$

$$q(z, t=0) = 1, \tag{2.23}$$

where ε_0 is the initial amplitude of the disturbance, and k is the non-dimensional axial wavenumber. The value of ε_0 is supposed to be small. In the calculation we take $\varepsilon_0 = 0.05$.

Due to periodicity and symmetry, only a half-wavelength segment of the jet is calculated. At the ends of the segment $z = 0$ and $z = \lambda/2$, where $\lambda = 2\pi/k$ is the wavelength of the disturbance, the following periodic boundary conditions are used:

$$\frac{\partial h}{\partial z}(z=0, t) = \frac{\partial h}{\partial z}\left(z=\frac{\lambda}{2}, t\right) = 0, \tag{2.24}$$

$$u(z=0, t) = u\left(z=\frac{\lambda}{2}, t\right) = 0, \tag{2.25}$$

$$\frac{\partial \tau_{zz}}{\partial z}(z=0, t) = \frac{\partial \tau_{zz}}{\partial z}\left(z=\frac{\lambda}{2}, t\right) = 0, \tag{2.26}$$

$$\frac{\partial \tau_{rr}}{\partial z}(z=0, t) = \frac{\partial \tau_{rr}}{\partial z}\left(z=\frac{\lambda}{2}, t\right) = 0, \tag{2.27}$$

$$\frac{\partial q}{\partial z}(z=0, t) = \frac{\partial q}{\partial z}\left(z=\frac{\lambda}{2}, t\right) = 0, \tag{2.28}$$

$$\frac{\partial \phi_{,a}}{\partial z}(r, z=0, t) = \frac{\partial \phi_{,a}}{\partial z}\left(r, z=\frac{\lambda}{2}, t\right) = 0. \tag{2.29}$$

3. Numerical results

A hybrid algorithm is used to solve the coupled flow field and electric field in this problem. That is, the 1-D equations (2.14)–(2.19) are solved using an implicit finite-difference scheme with adaptive mesh refinement technique, and the Laplace equation (2.7) is solved using the boundary element method with the boundary conditions (2.8), (2.12), (2.13) and (2.29). The procedure is as follows: first, the normal electric fields E_n and E_{an} and the tangential electric field E_t at time $t = t_n$ are assigned to the discretized 1-D equations (the momentum equation and the surface charge conservation equation) to calculate the jet radius h, the axial velocity u, the polymeric stress components τ_{zz} and τ_{rr} and the surface charge density q at time $t = t_{n+1}$; then, the obtained jet radius h and surface charge density q are used in the boundary conditions of the electric field to calculate the electrical potentials at $t = t_{n+1}$; subsequently, the electric fields E_n, E_{an} and E_t at $t = t_{n+1}$ are calculated and substituted into the 1-D equations to update the values of h, u, τ_{zz}, τ_{rr} and q at $t = t_{n+1}$. The iteration goes on until all the quantities converge to a requested accuracy. The calculation is stopped when the minimum radius of the jet drops below 0.01 for beads-on-a-string structures or the quantities alter too violently for spike or quasi-spike structures. The validity of the code has been checked by comparing with the results in Li *et al.* (2016).

The values of the dimensionless parameters are estimated in the following way. Consider a dilute polymer aqueous solution of density 1000 kg m^{-3}, zero-shear viscosity 0.01 Pa s, stress relaxation time 0.5 ms and surface tension 0.05 N m^{-1}. The radius of the jet is 100 μm. Thus we have $Oh = 0.14$ and $De = 3.5$. Recalling that the Ohnesorge number is essentially the ratio of the viscous–capillary time scale

https://doi.org/10.1017/jfm.2019.451 Published online by Cambridge University Press

$t_v = \eta_0 R/\sigma$ to the inertia–capillary time scale t_c (Turkoz *et al.* 2018), a value as small as 0.14 indicates that viscosity is a factor less important than surface tension in the situation considered here. The Deborah number is the ratio of the stress relaxation time λ to the capillary time t_c, and a value of 3.5 indicates that elasticity is comparable to capillarity. As to the solvent to solution viscosity ratio, with loss of generality, we take $\beta = 0.1$. In addition, the radius ratio of the grounded electrode to the jet, $b = R_0/R$, is set to 5. In the calculation these four dimensionless numbers (*Oh*, *De*, β and b) remain unchanged. What we are concerned about is the other four parameters, among which, the axial wavenumber k must be smaller than the corresponding cutoff wavenumber, the electrical Bond number χ varies from 0 to 0.8, the relative electrical permittivity ε_r ranges from 3 to 80 and the relative electrical relaxation time τ from 0.001 to 100.

3.1. *Linear instability of an electrically charged, poorly conducting, viscoelastic liquid jet*

Linearizing the 1-D equations (2.14)–(2.19) and substituting the following normal mode decomposition into them,

$$h = 1 + \hat{h}\exp(\omega t + \mathrm{i}kz), \tag{3.1}$$
$$u = \hat{u}\exp(\omega t + \mathrm{i}kz), \tag{3.2}$$
$$\tau_{zz} = \hat{\tau}_{zz}\exp(\omega t + \mathrm{i}kz), \tag{3.3}$$
$$\tau_{rr} = \hat{\tau}_{rr}\exp(\omega t + \mathrm{i}kz), \tag{3.4}$$
$$q = 1 + \hat{q}\exp(\omega t + \mathrm{i}kz), \tag{3.5}$$

where the hat denotes the initial amplitude of the disturbance, ω is the complex frequency with the real part ω_r the temporal growth rate and the imaginary part ω_i the speed of wave propagation and i is the imaginary unit, one obtains the dispersion relation

$$\omega\left(\omega + 3\beta Ohk^2 + \frac{3(1-\beta)Ohk^2}{1+\omega De} + \frac{\chi\Xi k^2(2+k\Delta)}{\omega\zeta + \tau\varepsilon_r}\right) - \frac{1}{2}k^2(1-k^2) + \chi k^2\frac{\xi}{\zeta}\left(\varepsilon_r + 2\Xi - \frac{\tau\varepsilon_r\Xi(2+k\Delta)}{\omega\zeta + \tau\varepsilon_r}\right) = 0, \tag{3.6}$$

where

$$\Delta = \frac{I_1(k)K_0(kb) + K_1(k)I_0(kb)}{I_0(k)K_0(kb) - K_0(k)I_0(kb)}, \quad \xi = 1 + k\Delta, \quad \zeta = \varepsilon_r - \frac{I_0(k)}{I_1(k)}\Delta, \quad \Xi = \frac{I_0(k)}{kI_1(k)}, \tag{3.7a–d}$$

$I_n(x)$ and $K_n(x)$, $n = 0, 1$, are the nth-order modified Bessel functions of the first and second kinds, respectively. Letting $\tau\varepsilon_r \to \infty$ in (3.6), one gets the dispersion relation for the perfectly conducting case,

$$\omega\left(\omega + 3\beta Ohk^2 + \frac{3(1-\beta)Ohk^2}{1+\omega De}\right) - \frac{1}{2}k^2(1 - k^2 - 2\chi(1+k\Delta)) = 0. \tag{3.8}$$

Further, in the absence of an electric field, equation (3.8) reduces to that for a non-electrified viscoelastic liquid jet, i.e.

$$\omega\left(\omega + 3\beta Ohk^2 + \frac{3(1-\beta)Ohk^2}{1+\omega De}\right) - \frac{1}{2}k^2\left(1 - k^2\right) = 0. \tag{3.9}$$

https://doi.org/10.1017/jfm.2019.451 Published online by Cambridge University Press

If $De = 0$ in (3.6), (3.8) or (3.9), these dispersion relations become the corresponding ones for purely viscous liquid jets.

Abandoning the slender body approximation, one can derive a dispersion relation for the 2-D linear instability of the jet. Substituting the normal mode decomposition into the governing equations and boundary conditions (2.1)–(2.12) and omitting the high-order terms, one obtains a set of linear homogeneous equations. To ensure the equations have non-trivial solutions, the determinant of the coefficient matrix should be zero, which yields the dispersion relation (Li, Yin & Yin 2011)

$$\begin{vmatrix} kI_1(k) & \mathrm{i}I_1(l) & 0 & -\omega \\ 2\mathrm{i}kI_1(k) & -\left(1+\dfrac{l^2}{k^2}\right)I_1(l) & \dfrac{2\mathrm{i}\chi I_0(k)}{kC^*\zeta I_1(k)} & \dfrac{2\mathrm{i}\chi I_0(k)}{kC^*\zeta I_1(k)}\xi \\ -\omega I_0(k) - 2C^*k^2 I_1'(k) & -2\mathrm{i}C^*lI_1'(l) & 2\chi\left(1-\dfrac{\varepsilon_r}{\zeta}\right) & 1-k^2-\dfrac{2\chi\varepsilon_r\xi}{\zeta} \\ -k^2 I_1'(k) & -\mathrm{i}lI_1'(l) & \omega+\dfrac{\varepsilon_r\tau}{\zeta} & \dfrac{\varepsilon_r\tau\xi}{\zeta} \end{vmatrix} = 0, \tag{3.10}$$

where

$$C^* = Oh\frac{1+\beta\omega De}{1+\omega De}, \quad l = \sqrt{k^2+\frac{\omega}{C^*}}, \tag{3.11a,b}$$

in which the prime denotes the first derivative of the Bessel function with respect to the argument, i.e. $I_1'(x) = I_0(x) - 1/xI_1(x)$. Ruo *et al.* (2012) considered a more complicated model taking into account the effect of the inertial force, the surrounding gas and a constant basic axial elastic tension. Mohamed *et al.* (2015) investigated the transition from convective to absolute instability of a viscoelastic jet in the presence of unrelaxed axial elastic tension, and they pointed out that the effects of the unrelaxed tension were not accounted for correctly in Ruo *et al.* (2012). On the other hand, some simpler models can be directly obtained from (3.10). For instance, if the product of τ and ε_r approaches infinity, the dispersion relation (3.10) reduces to the one for perfectly conducting, viscoelastic liquid jets (Li *et al.* 2011; Yang, Liu & Fu 2012; Li *et al.* 2016). If De is equal to zero, the parameter C^* in (3.10) is replaced by Oh, and the dispersion relation becomes the one for poorly conducting, purely viscous liquid jets as derived by López-Herrera, Riesco-Chueca & Gañán-Calvo (2005).

The comparison of the 1-D slender body approximation with the 2-D result is shown in figure 2. As shown in the figure, both the 1-D and 2-D results predict the suppression of the electric field to the temporal growth rate ω_r at small wavenumbers. However, the 1-D approximation overestimates the suppression effect of the electric field.

3.2. *Different structures and their domains in the k–χ plane*

Four different structures are detected in the simulation, i.e. the beads-on-a-string structure with satellite droplets, the beads-on-a-string with no satellite droplets, the quasi-spike structure and the spike structure. The profiles of these structures are shown in figure 3(*b–e*), respectively. As illustrated in the figure, for the beads-on-a-string structure with no satellite droplets, the jet evolves into a morphology of main droplets connected by a fine filament. For the beads-on-a-string structure with satellite droplets, small secondary droplets appear between large primary ones. The singular spike

https://doi.org/10.1017/jfm.2019.451 Published online by Cambridge University Press

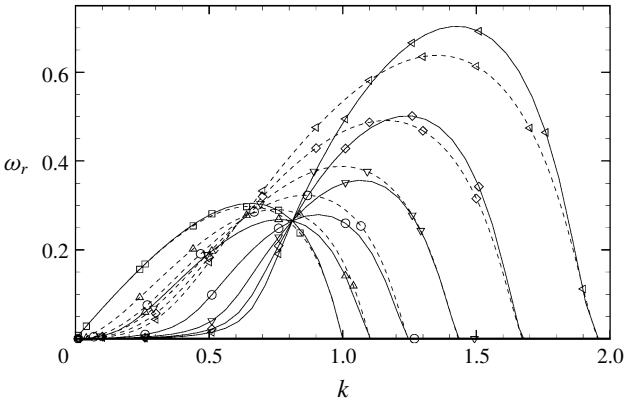

FIGURE 2. The temporal growth rate ω_r versus the axial wavenumber k for different values of the electrical Bond number χ, $\chi = 0$ (□), 0.2 (△), 0.4 (○), 0.6 (▽), 0.8 (◇) and 1.0 (◁). The solid lines are the 1-D results, and the dashed lines are the 2-D results. $Oh = 0.14$, $\beta = 0.1$, $De = 3.5$, $\varepsilon_r = 3$, $\tau = 0.1$, $b = 5$.

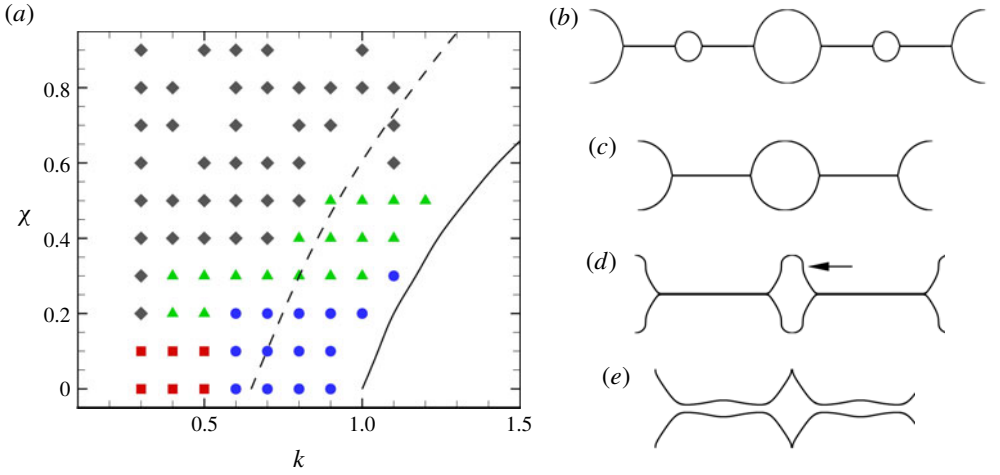

FIGURE 3. (Colour online) (*a*) The domains in the k-χ plane. The symbols represent the data points being calculated. Squares: the beads-on-a-string structure with satellite droplets; circles: the beads-on-a-string structure with no satellite droplets; triangles: the quasi-spike structure; diamonds: the spike structure. Solid line: the fitted result of the cutoff wavenumbers; dashed line: the fitted result of the most unstable wavenumbers, according to linear theory. $Oh = 0.14$, $\beta = 0.1$, $De = 3.5$, $\varepsilon_r = 3$, $\tau = 0.1$, $b = 5$. The profiles of (*b*) the beads-on-a-string structure with satellite droplets, (*c*) the beads-on-a-string structure with no satellite droplets, (*d*) the quasi-spike structure and (*e*) the spike structure. In (*b–e*), a two-wavelength segment of the jet is plotted.

structure is characterized by pointed spikes quickly formed before the jet undergoes unidirectional elongation. The quasi-spike structure also exhibits singularity, for which the shape of the droplets becomes abnormal, like a blunt spike, with an almost infinite slope at some points (see where the arrow points at in figure 3(*d*)). Further development of the quasi-spike structure cannot be predicted by the present 1-D

https://doi.org/10.1017/jfm.2019.451 Published online by Cambridge University Press

model, for the 1-D model prohibits infinite slopes and requires that the quantities h, u, τ_{zz}, τ_{rr} and q be single-valued functions of the axial coordinate z. From a physical point of view, the quasi-spike structure can be regarded as a transitional morphology between the beads-on-a-string and the spike structures. It was not found in the previous study of perfectly conducting jets (Li *et al.* 2016, 2017*b*). Therefore its formation is naturally attributed to finite conductivity of the liquid.

The domains of the structures in the k–χ plane are shown in figure 3(*a*). In the parametric plane, the beads-on-a-string structure with satellite droplets is located at small axial wavenumbers and small electrical Bond numbers. When k exceeds 0.5, satellite droplets disappear and only main droplets stay on the filament. The quasi-spike or spike structure may arise at a value of the electrical Bond number χ as small as 0.2. When χ is increased to 0.4, the beads-on-a-string structure disappears over all axial wavenumbers. When χ is further increased to 0.6, only the spike structure exists. In general, the existence of the electric field damages beads-on-a-string structures and leads to the formation of quasi-spike or spike structures, and obviously the charge level does not necessarily have to be high.

To reveal the mechanisms in the formation of different structures, the properties of the jet at the late stages are shown in figure 4, where the axial wavenumber $k = 0.8$. In the figure, due to periodicity and symmetry, the physical quantities are illustrated only over a half-wavelength distance in the axial direction. In the left column, the electric field is small ($\chi = 0.2$), and a beads-on-a-string structure with no satellite droplets is developed; in the middle column, χ is increased to 0.4, and a quasi-spike structure is formed; in the right column, where χ is as large as 0.8, a spike structure is observed. For the beads-on-a-string structure, the filament undergoes uniaxial elongation and the jet is fully stretched. The liquid in the filament is directed into the droplet continuously, the thickness of the filament decreases monotonically and the droplet oscillates periodically. For the quasi-spike structure, an irregular droplet with a relatively thick filament is formed. The droplet experiences no oscillation and is elongated monotonically in the radial direction. For the spike structure, the droplet becomes more irregular with a pointed spike. For the beads-on-a-string structure, the axial elongation results in a large first normal stress difference $\tau_{zz} - \tau_{rr}$ in the filament. For the spike structure, the first normal stress difference in the entire jet is small.

As shown in the figure, the distributions of the electric fields are quite different in three structures. Particularly, in the beads-on-a-string structure, the normal electric field E_{an} is large and increases mildly towards the peak of the droplet; in the quasi-spike structure, E_{an} is larger and increases more rapidly towards the peak; in the spike structure, E_{an} increases much more rapidly and becomes much larger at the peak. Another difference lies in the tangential electric field E_t, which is visibly non-zero in the filament of the beads-on-a-string structure, near the peak of the droplet of the spike structure and becomes non-negligible in both the droplet and the filament of the quasi-spike structure. As a result, in the beads-on-a-string structure, a non-zero tangential electrostatic force f_{et} exists in the filament, which is particularly large in the corner region joining the droplet to the filament. It serves as a resistance force, preventing the liquid in the filament from getting into the droplet and hindering the thinning of the filament. The electrostatic pressure p_e is negligible in the whole jet, and the capillary force p_σ is responsible for the formation of the beads-on-a-string structure. The great jump of the electro-capillary pressure $p_\sigma + p_e$ in the corner region results in a large negative pressure gradient there, which results in the continuous drainage of the filament. For the quasi-spike structure, the electro-capillary pressure $p_\sigma + p_e$ in the droplet is small, whereas the tangential electrostatic force f_{et} is extremely large at

https://doi.org/10.1017/jfm.2019.451 Published online by Cambridge University Press

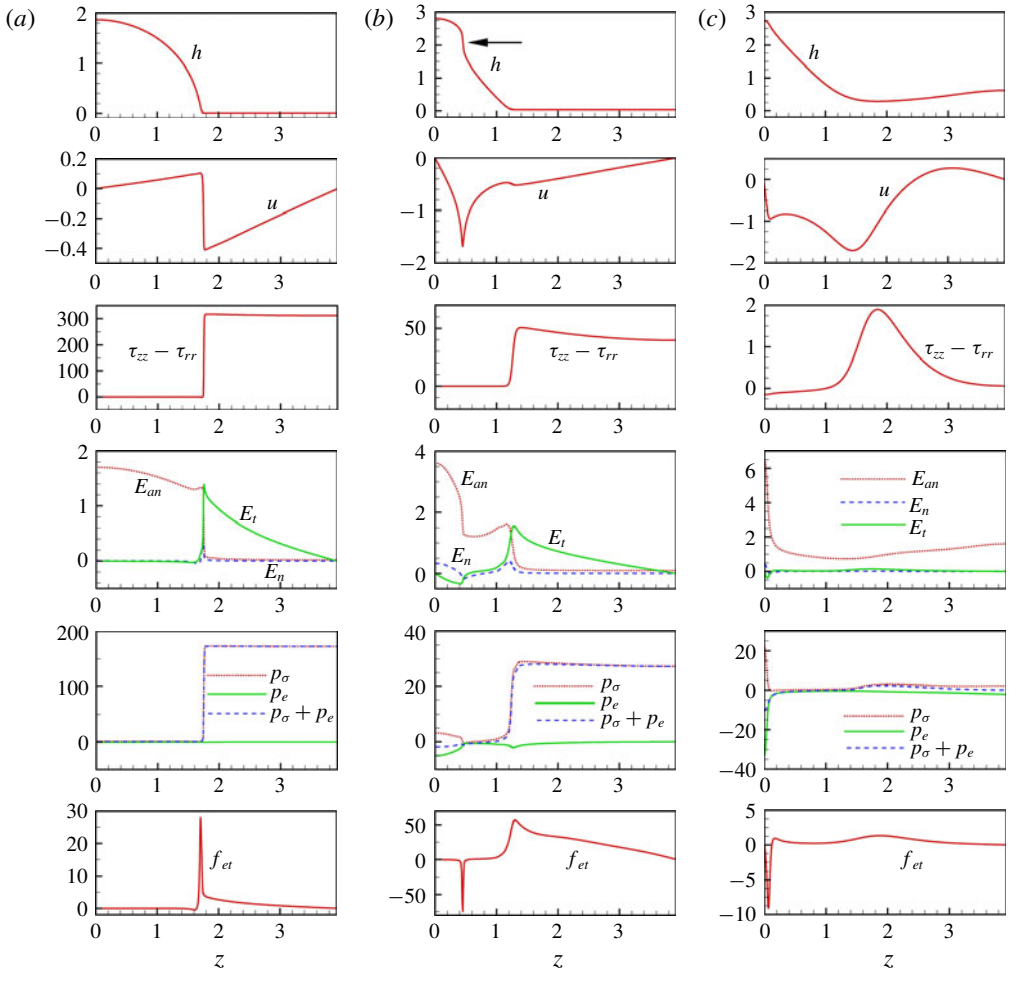

FIGURE 4. (Colour online) Comparison between different structures, where h is the jet radius, u is the axial velocity, $\tau_{zz} - \tau_{rr}$ is the first normal stress difference, E_n is the normal electric field intensity, E_t is the tangential electric field intensity, p_σ is the capillary pressure, p_e is the electrostatic pressure, $p_\sigma + p_e$ is the electro-capillary pressure and f_{et} is the tangential electrostatic force. Due to periodicity and symmetry, only a half-wavelength segment of the jet is shown. (*a*) The beads-on-a-string structure with no satellite droplets at time $t = 45$, $\chi = 0.2$, $k = 0.8$, $\varepsilon_r = 3$, $\tau = 0.1$; (*b*) the quasi-spike structure at $t = 27.05$, $\chi = 0.4$, $k = 0.8$, $\varepsilon_r = 3$, $\tau = 0.1$; (*c*) the spike structure at $t = 8.131$, $\chi = 0.8$, $k = 0.8$, $\varepsilon_r = 3$, $\tau = 100$. $Oh = 0.14$, $\beta = 0.1$, $De = 3.5$, $b = 5$.

the singular point where the slope of the droplet surface rises abruptly. This tangential electrostatic force acts to push the liquid towards the peak and promotes the formation of the quasi-spike structure. In the study of perfectly conducting jets (Li *et al.* 2017*b*), the jet is equipotential all the time and the tangential electrostatic force is absent, and as a consequence the quasi-spike structure is not formed. For the spike structure, the electrostatic pressure p_e can be very large in the neighbourhood of the peak. So is the capillary pressure p_σ, but with the opposite sign. The interplay of the capillary and electrostatic forces, with a negative gradient near the peak, tries to enhance the radial

https://doi.org/10.1017/jfm.2019.451 Published online by Cambridge University Press

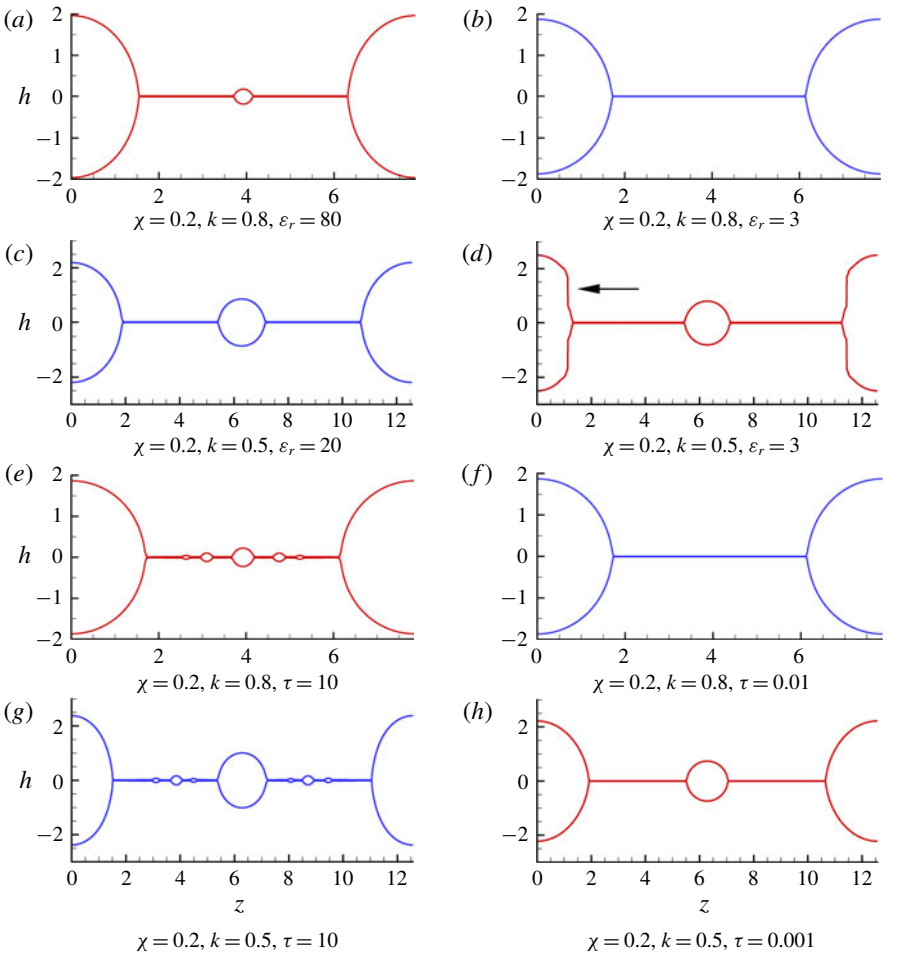

FIGURE 5. (Colour online) Effect of finite conductivity on the transition between structures: (*a–d*) $\tau = 0.1$; (*e–h*) $\varepsilon_r = 3$. $Oh = 0.14$, $\beta = 0.1$, $De = 3.5$, $b = 5$.

deformation of the droplet. The negative tangential electrostatic force f_{et} accelerates the formation of the spike structure as well. In general, the tangential electric field appears to play different roles in the formation of different structures: it hinders the thinning of the filament in the beads-on-a-string structure, accounts for the emergence of the quasi-spike structure and accelerates the formation of the spike structure.

3.3. *Effect of finite conductivity on the beads-on-a-string structure*

In this 1-D model, finite conductivity is represented by two dimensionless parameters, i.e. the relative electrical permittivity ε_r and the relative electrical relaxation time τ. The larger the product of ε_r and τ, the larger the conductivity of the liquid. The calculation result shows that varying the value of ε_r or τ may influence the formation of the beads-on-a-string structure. For instance, decreasing ε_r may shrink satellite droplets or eliminate them entirely, as shown in figure 5(*a*,*b*). In addition, decreasing ε_r may lead to the collapse of the beads-on-a-string structure and the emergence of the quasi-spike structure, as shown in figure 5(*c*,*d*). Decreasing τ may

https://doi.org/10.1017/jfm.2019.451 Published online by Cambridge University Press

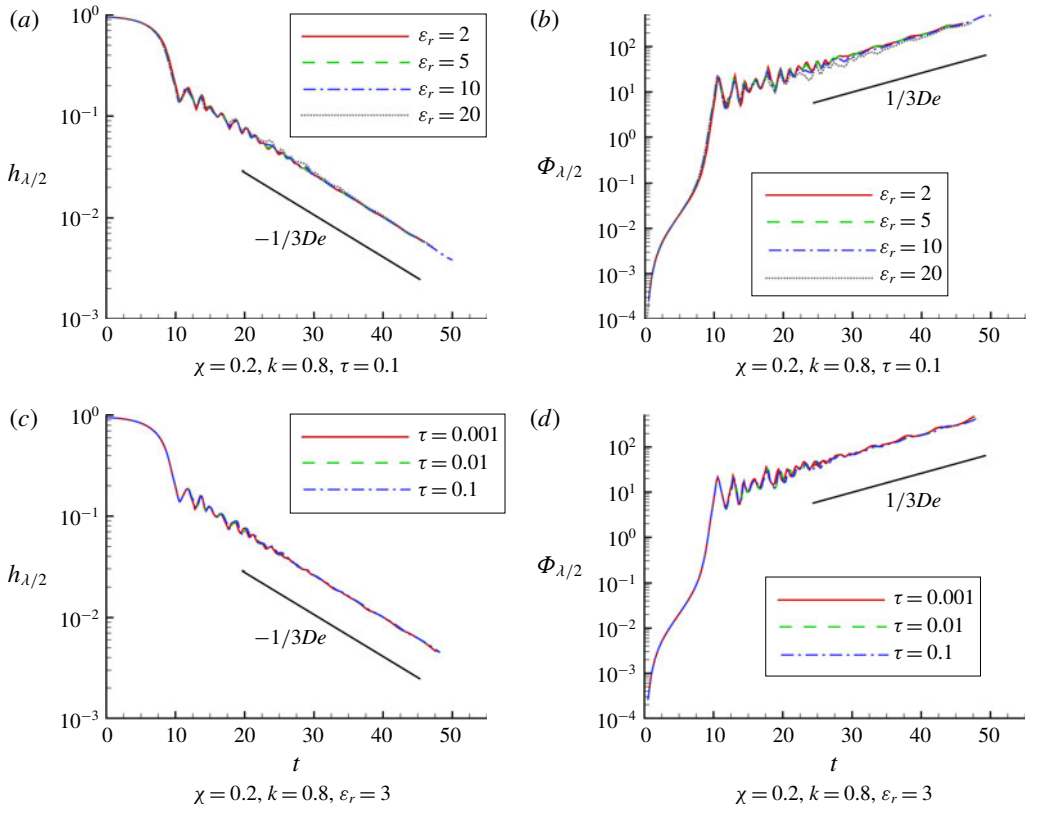

FIGURE 6. (Colour online) Time evolution of (*a*,*c*) the jet radius h, and (*b*,*d*) the first normal stress difference $\Phi(=\tau_{zz}-\tau_{rr})$ at the midpoint of the filament. $Oh = 0.14$, $\beta = 0.1$, $De = 3.5$, $b = 5$.

also remove secondary or higher-order droplets from a beads-on-a-string structure, see figure 5(*e*–*h*).

In our previous study of perfectly conducting viscoelastic liquid jets (Li *et al.* 2016), we found that under the action of the radial electric field, the decrease in the filament thickness and the increase in the first normal stress difference deviate a little from (are slower than) the $1/3De$ exponential law of the non-electrified jets (Chang *et al.* 1999; Clasen *et al.* 2006; Ardekani *et al.* 2010). Unexpectedly, here the thinning of leaky dielectric liquid jets is another scenario. As shown in figure 6, for a poorly conducting liquid jet, the filament thins with time, basically following the $1/3De$ law. Moreover, varying the value of ε_r or τ influences the trend little. This is understandable, considering that in the finite conductivity case, the electrostatic pressure p_e is extremely small in the entire jet; the tangential electrostatic force f_{et} is non-zero, but compared with the large gradients of the capillary pressure p_σ and the first normal stress difference $\tau_{zz}-\tau_{rr}$ at the corner joining the droplet to the filament, it is of secondary importance (see figure 4(*a*)).

In the beads-on-a-string structure, due to the interplay between viscoelastic, inertial, capillary and electrostatic forces, the droplets undergo periodic oscillations with time-decreasing amplitude. The effect of finite conductivity on the oscillation of the main droplets is shown in figure 7, where the radius of the jet at the peak position,

https://doi.org/10.1017/jfm.2019.451 Published online by Cambridge University Press

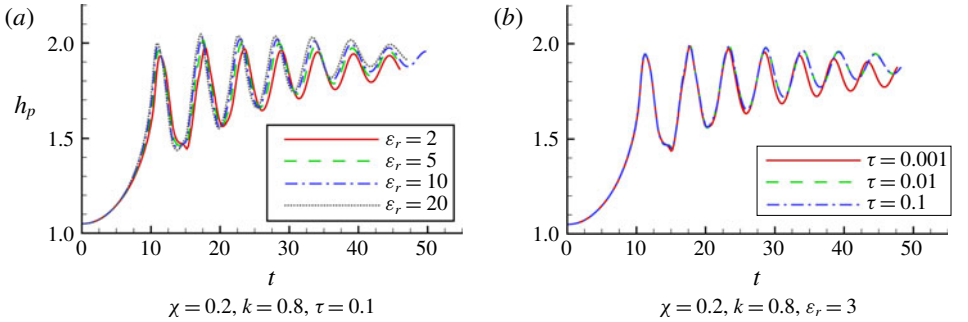

FIGURE 7. (Colour online) Effect of (*a*) the relative electrical permittivity ε_r and (*b*) the relative electrical relaxation time τ on the time evolution of the jet radius at the peak h_p. $Oh = 0.14,\ \beta = 0.1,\ De = 3.5,\ b = 5$.

ε_r	2	5	10	20	3	3	3
τ	0.1	0.1	0.1	0.1	0.001	0.01	0.1
t_{1D}	5.22	5.30	5.32	5.53	4.96	5.24	5.24

TABLE 1. The period of oscillation of the droplet, t_{1D}, for different values of the relative electrical permittivity ε_r and the relative electrical relaxation time τ, extracted from figure 7.

h_p, is drawn as a function of time t. It can be seen in the figure that as ε_r or τ increases, both the amplitude and the period of oscillation of the droplet increase slightly. The period of oscillation, t_{1D}, is extracted from the figure and collected in table 1. According to linear theory, for an isolated viscoelastic liquid droplet of the same volume, in the absence of an electric field, the period of oscillation is approximately 5.22 (Khismatullin & Nadim 2001; Brenn & Teichtmeister 2013; Li, Yin & Yin 2017*a*). In the beads-on-a-string structure, Li *et al.* (2017*a*) detected that the period of oscillation of the droplet decreases with time due to the existence of the filament, which exerts an extra time-increasing resistance force on the droplet. The resistance force leads to an increase in energy dissipation in the droplet. For a purely viscous droplet, with the increase in energy dissipation, the frequency of oscillation of the droplet is decreased. However, for a non-Newtonian viscoelastic liquid droplet, the frequency of oscillation can be increased (Brenn & Teichtmeister 2013). By contrast, as shown in table 1, in the presence of the electric field, the period of oscillation is larger than that of its non-electrified counterpart in most situations. The electric field is the only possible factor accounting for this opposite tendency. In addition, the tendency that increasing ε_r or τ slightly increases the period of oscillation is coincident with that found in the study of oscillations of isolated electrically charged viscoelastic droplets of finite conductivity (Li, Yin & Yin 2019).

3.4. *Effect of finite conductivity on the spike structure*

Typical evolution of the spike structure is shown in figure 8, where the shape of the jet is drawn for a sequence of time instants. As shown in the figure, when sharp spikes are formed, the jet is still thick everywhere, there being no thin filament visible. The spikes exhibit a self-similar characteristic. The similarity in the spike structure has

https://doi.org/10.1017/jfm.2019.451 Published online by Cambridge University Press

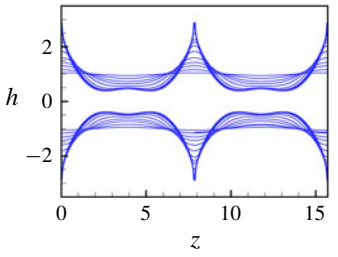

FIGURE 8. (Colour online) Formation of the spike structure; $\chi = 0.8$, $k = 0.8$, $\varepsilon_r = 10$, $\tau = 0.1$, $Oh = 0.14$, $\beta = 0.1$, $De = 3.5$, $b = 5$.

been examined by Wang *et al.* (2009) for the highly viscous case and by Li *et al.* (2017*b*) for the viscoelastic case.

The effect of finite conductivity on the time evolution of the spike structure is illustrated in figure 9, for the axial wavenumber $k = 0.8$ and the electrical Bond number $\chi = 0.8$. As shown in figure 9(*a*,*b*), linear theory predicts that the temporal growth rate ω_r increases slightly with ε_r or τ increasing, indicating that the jet is more unstable for larger ε_r or τ. The tendency at the nonlinear stages is similar. As shown in figure 9(*c*,*d*), the radius of the jet at the peak position, h_p, increases faster at larger values of ε_r or τ. That is, increasing the conductivity of the liquid accelerates the formation of the spike structure. In these two plots, the linear results are also shown (the dashed lines) for comparison.

To better understand the effect of finite conductivity on the development of the spike structure, the distributions of the electro-capillary pressure $p_\sigma + p_e$ and the tangential electrostatic force f_{et} along the z axis at different time instants $t = 3, 5, 7$ are illustrated in figure 9(*e*–*j*), for different values of ε_r and τ. It can be seen that both $p_\sigma + p_e$ and f_{et} increase with time, regardless of the value of ε_r or τ. Relatively, the tangential electrostatic force f_{et} grows much faster. At $t = 3$, f_{et} is approximately one order of magnitude smaller than the electro-capillary pressure gradient. As time proceeds, f_{et} becomes comparable to the gradient of $p_\sigma + p_e$ (see the lines for $t = 7$). Spatially, in most situations, the electro-capillary pressure $p_\sigma + p_e$ increases monotonically along the z axis, resulting in a negative pressure gradient which drives the flow towards the peak and promotes the deformation of the jet. Moreover, as ε_r or τ increases, $p_\sigma + p_e$ varies more mildly along the z axis, indicating that the electro-capillary pressure gradient is larger for less conducting liquids. The tangential electrostatic force also decreases as ε_r or τ increases, much faster than the electro-capillary pressure gradient. When ε_r is as large as 80 or τ as large as 100, f_{et} can even become negative at large times, as shown in figure 9(*i*,*j*), serving as a force pushing the liquid towards the peak. Nevertheless, f_{et} is generally greater than zero. Different from the negative gradient of the electro-capillary pressure, this positive tangential electrostatic force tends to drive the flow away from the peak and inhibit the deformation of the jet. Due to the suppressing effect of the tangential electrical force on jet deformation, the spike structure forms more slowly for less conducting liquids, as shown in figure 9(*c*,*d*). In § 3.2, we conclude that the tangential electrical force accelerates the formation of spike structure. The results shown in figure 9 seem to be against this statement. But in § 3.2 what we examine is the late stages of the evolution of the spike structure, and here it is the early stages prior to the rapid increase in jet radius at the peak position. There is no paradox. These findings just reflect that the tangential electrical

https://doi.org/10.1017/jfm.2019.451 Published online by Cambridge University Press

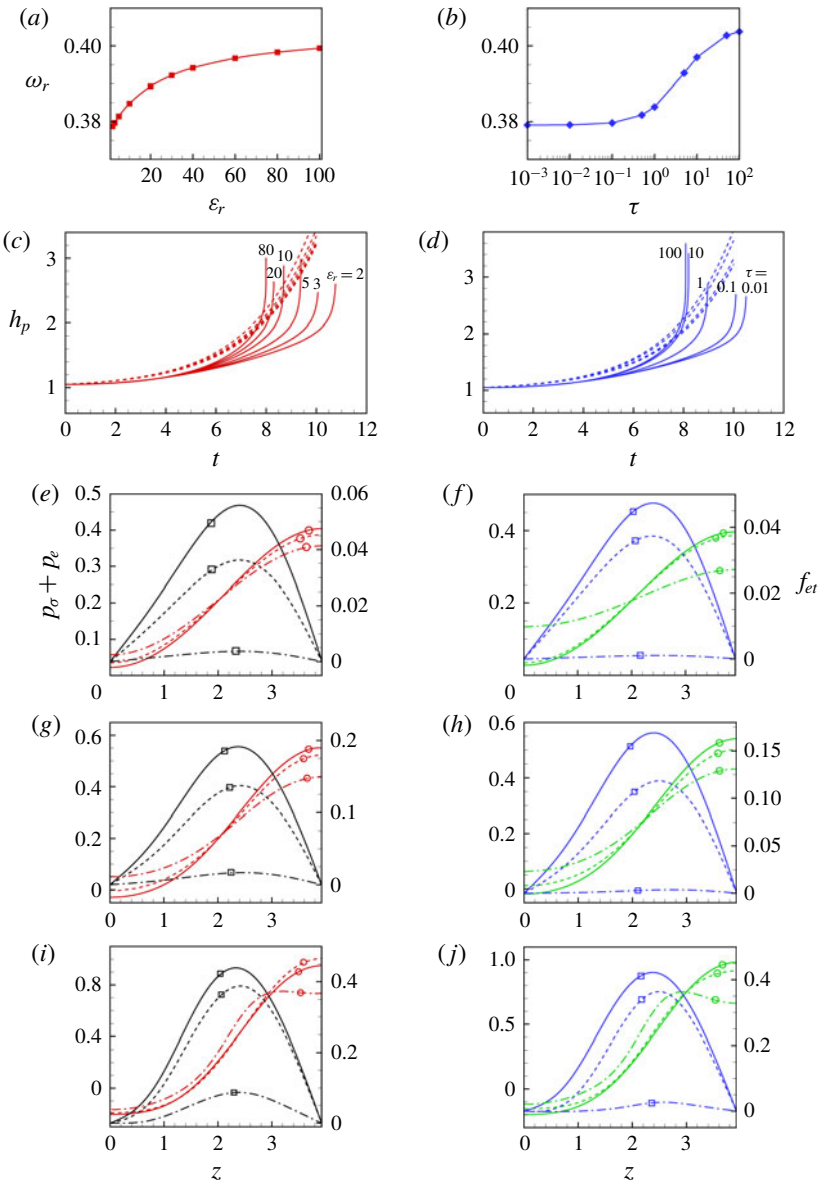

FIGURE 9. (Colour online) Effect of finite conductivity on the evolution of the spike structure. Variation of the temporal growth rate ω_r with (*a*) the relative electrical permittivity ε_r and (*b*) the relative electrical relaxation time τ, according to linear theory. Time evolution of the radius of the jet at the peak, h_p, for different values of (*c*) ε_r and (*d*) τ. (*e–j*) Distributions of the electro-capillary pressure $p_\sigma + p_e$ (lines with a circle) and the tangential electrostatic force f_{et} (lines with a square) at different time instants, (*e*,*f*) $t = 3$, (*g*,*h*) $t = 5$, (*i*,*j*) $t = 7$. In (*e*,*g*,*i*), the results for $\varepsilon_r = 2$ (solid lines), 5 (dashed lines), 80 (dash-dotted lines) and $\tau = 0.1$ are represented; in (*f*,*h*,*j*), the results for $\tau = 0.1$ (solid lines), 1 (dashed lines), 100 (dash-dotted lines) and $\varepsilon_r = 3$ are represented. $\chi = 0.8$, $k = 0.8$, $Oh = 0.14$, $\beta = 0.1$, $De = 3.5$, $b = 5$.

https://doi.org/10.1017/jfm.2019.451 Published online by Cambridge University Press

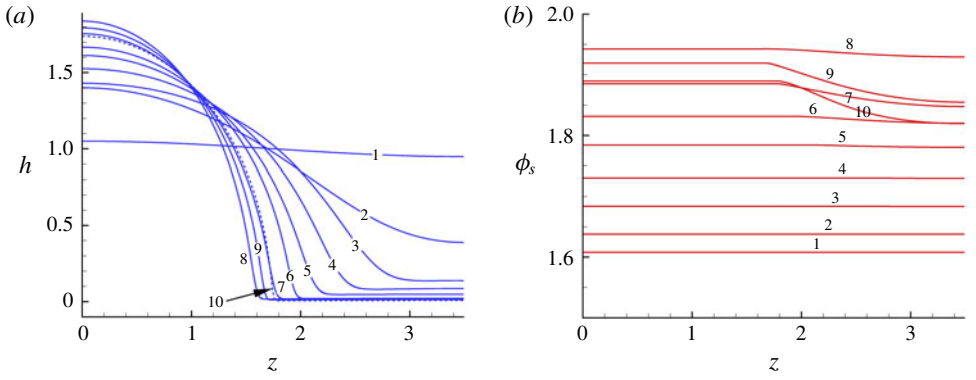

FIGURE 10. (Colour online) Variation of (*a*) the shape of the jet and (*b*) the electrical potential at the surface of the jet, ϕ_s, for a sequence of time instants (numbered from 1 to 10) during the evolution process of the beads-on-a-string structure with no satellite droplets, the case of large conductivity, $\varepsilon_r = 80$, $\tau = 100$. $\chi = 0.1$, $k = 0.9$, $Oh = 0.14$, $\beta = 0.1$, $De = 3.5$, $b = 5$.

force plays different roles at the early and late stages during the evolution of the spike structure.

3.5. *Difference between the finite conductivity, large conductivity, infinite conductivity and constant-voltage cases*

The finite conductivity case refers to the leaky dielectric model studied in this work, in which the conductivity of the liquid is moderate or poor, i.e. $\tau\varepsilon_r$ has a small limited value. In the large conductivity case, $\tau\varepsilon_r$ is large but still limited, where the leaky dielectric theory applies. The infinite conductivity case is the limit of the large conductivity case when $\tau\varepsilon_r$ approaches infinity. In the infinite conductivity case, the liquid is practically a perfect conductor. Over a distance of one wavelength in the axial direction, all the finite, large and infinite conductivity cases obey the conservation law of surface charge given by (2.4), but the electrical potential at the surface of the jet varies as the jet deforms. In Li *et al.* (2016, 2017*b*), the liquid is a perfect conductor and a constant voltage is imposed on the jet (which is referred to as the constant-voltage case). In such a case, as the jet deforms, the electrical potential of the jet remains unchanged, but charges are not conserved within a one-wavelength distance, different from the infinite conductivity case here. For a perfectly conducting liquid jet, surface charge conservation seems incompatible with constant electrical potential, owing to the fact that the jet is deforming.

Figure 10 shows the shape of the jet and the electrical potential at the surface of the jet at different time instants during the evolution of the beads-on-a-string structure with no satellite droplets, for the large conductivity case $\varepsilon_r = 80$ and $\tau = 100$. Clearly, at the initial time $t = 0$ (the line labelled '1'), the electrical potential at the surface of the jet, ϕ_s, is uniform with a value of 1.6094 (i.e. $\ln b$ with $b = 5$), equal to that of the corresponding constant-voltage case. At the times labelled '2', '3' and '4', the surface of the jet remains equipotential but the potential is not equal to the initial value anymore. At the larger times labelled '5' to '10', the jet becomes visibly non-equipotential. Based on the tendency illustrated in figure 10, it is predicted that in the infinite conductivity case the jet remains equipotential at larger deformations, but the potential at the jet surface varies with time, different from the constant-voltage case.

https://doi.org/10.1017/jfm.2019.451 Published online by Cambridge University Press

The comparison of the finite conductivity case with the large conductivity case is shown in figure 11, for the electrical Bond number $\chi = 0.3$ and the axial wavenumber $k = 0.6$. (*a*) shows the properties of the jet in the finite conductivity case $\varepsilon_r = 3$, $\tau = 0.1$, and (*b*) shows the results for the large conductivity case $\varepsilon_r = 80$, $\tau = 100$. In the large conductivity case, a beads-on-a-string structure with satellite droplets is developed. By contrast, in the finite conductivity case, satellite droplets disappear, and main droplets are deformed and elongated in the radial direction, with a quasi-spike structure ultimately formed. As illustrated in the figure, the distributions of the properties of the two structures, such as the axial velocity, the first normal stress different, the normal and tangential electric fields, as well as the forces, are quite different from each other. In particular, the surface charge density q in the filament is much larger than that in the droplet in the large conductivity case, whereas in the finite conductivity case, the surface charge density in the droplet is large and in the filament is nearly zero. The difference of the normal electric field E_{an} between the two cases is similar. In the finite conductivity case, the electrostatic pressure p_e is small everywhere, but in the large conductivity case, it can be large in the filament. In the large conductivity case, the non-uniform electro-capillary pressure $p_\sigma + p_e$ in the filament exerts an extra drag force which intends to hinder the thinning of the filament as in the constant-voltage case (Li *et al.* 2016). In the finite conductivity case, a sharp pulse of the tangential electrostatic force f_{et} exists at the singular point with extremely large surface slope, which results in the formation of the quasi-spike structure. Differently, in the large conductivity case, the tangential electrostatic force in the droplet is negligible, but in the filament it can be large and basically acts as a drag during the thinning of the filament.

4. Experimental observation of spike structures

To the best of our knowledge, the singular spike structure resulting from the large radial elongation of droplets during the nonlinear evolution of an electrified viscous or non-Newtonian liquid jet has not been observed in experiments yet. Motivated by this, we perform a preliminary experimental observation of the spike structure. The schematic of the experimental set-up is shown in figure 12. In the experiment, a liquid jet is injected by a syringe into the air from a stainless steel needle of inner diameter 0.21 mm. The needle is connected to a high-voltage electric source. A high-speed camera with a macro lens in front of it is used to capture the motion of the jet. The frame rate is 10^5 fps. To facilitate the observation, two parallel plane grounded electrodes instead of an annular grounded electrode surround the needle at a distance of 5.5 mm (when the parallel plane electrodes are far enough away from the needle, the electric field is nearly radial).

Four different liquids are tested in the experiment: distilled water (small viscosity and large surface tension), ethanol (small viscosity and small surface tension), a mixture of ethanol and glycerol (large viscosity and small surface tension) and a slightly viscoelastic aqueous solution of polyethylene oxide (PEO, molecular weight 2×10^6). As shown in figures 13 and 14, for ethanol or the ethanol–glycerol mixture, whose surface tension is small, when an sufficiently large electric voltage is imposed on the jet, the continuous radial elongation of droplets and the resulting pointed spikes quite similar to those predicted by the 1-D model are observed in the experiment. However, for water or the viscoelastic PEO aqueous solution, whose surface tension is large, the formation of spikes is not observed, because corona discharge occurs before the electrostatic force is large enough to overcome the capillary force and trigger the

https://doi.org/10.1017/jfm.2019.451 Published online by Cambridge University Press

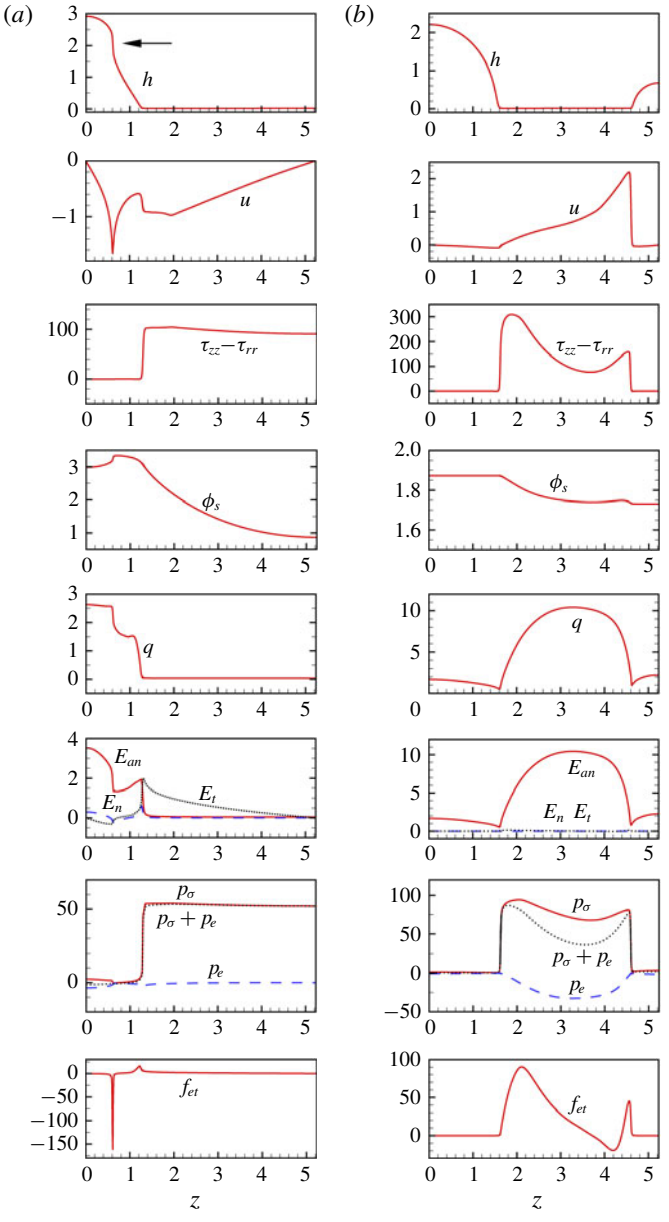

FIGURE 11. (Colour online) Comparison between the finite conductivity case $\varepsilon_r = 3$, $\tau = 0.1$ (a) and the large conductivity case $\varepsilon_r = 80$, $\tau = 100$ (b). In the figure, h is the jet radius, u is the axial velocity, $\tau_{zz} - \tau_{rr}$ is the first normal stress difference, ϕ_s is the electrical potential at the jet surface, q is the surface charge density, E_{an} is the normal electric field intensity in the air, E_n is the normal electric field intensity in the liquid, E_t is the tangential electric field intensity at the surface, p_σ is the capillary pressure, p_e is the electrostatic pressure, $p_\sigma + p_e$ is the electro-capillary pressure and f_{et} is the tangential electrostatic force. $\chi = 0.3$, $k = 0.6$, $Oh = 0.14$, $\beta = 0.1$, $De = 3.5$, $b = 5$.

https://doi.org/10.1017/jfm.2019.451 Published online by Cambridge University Press

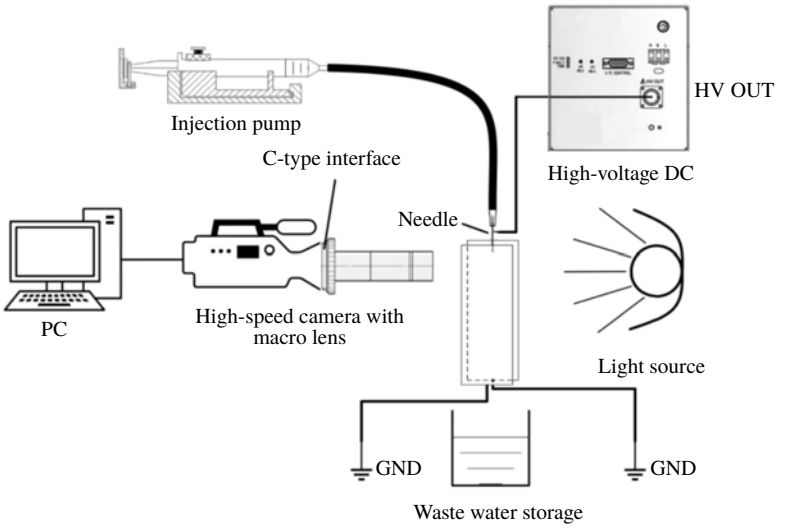

FIGURE 12. Schematic of the experimental set-up.

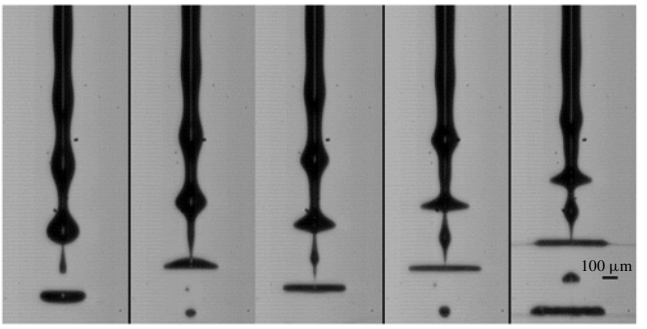

FIGURE 13. Formation of spike structure on the liquid jet of ethanol at electric voltage 6.3 kV and flow rate 2500 μl min^{-1}.

occurrence of spikes. In the future we will conduct a systematic experimental study on spike structures.

In addition, an interesting phenomenon observed in the experiment is the secondary break-up of a spike occurring at its periphery, as illustrated in figures (13) and (14). Also note that, prior to this secondary break-up, the spike may be fully elongated in the radial direction and develop an extremely oblate configuration, which is possibly due to the radial flow in it. A close-up in figure 15 clearly shows that tens of fine jets are emitted from the periphery of the spike. These jets undergo the Rayleigh instability and are expected to break up into super-small droplets ultimately, although the details of break-up and the resulting droplets are indiscernible in the figure due to the poor resolution. The second break-up of the spike structure and the subsequent atomization is apparently three-dimensional and cannot be predicted by a simplified 1-D model. It is of interest to study theoretically and experimentally this instability as well as the effect of the relevant factors including inertia, electric field and viscoelasticity on it. Many open problems remain in the formation and subsequent break-up of the spike structure.

https://doi.org/10.1017/jfm.2019.451 Published online by Cambridge University Press

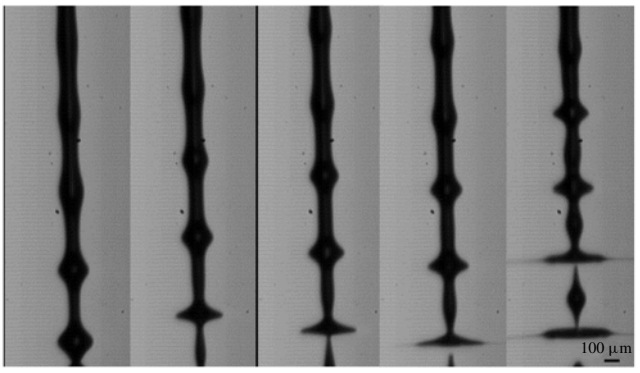

FIGURE 14. Formation of spike structure on the liquid jet of a mixture of ethanol and glycerol at electric voltage 6.4 kV and flow rate 3000 μl min^{-1}.

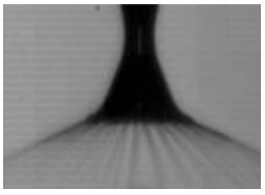

FIGURE 15. Secondary break-up of a spike with the emission of tens of ultra-fine jets from its periphery.

5. Conclusion

In this work a 1-D model is built to numerically study the nonlinear dynamics of an electrically charged viscoelastic liquid jet of finite conductivity. The effect of the charge level, axial wavenumber and finite conductivity on the nonlinear behaviour of the viscoelastic jet is explored. Four different structures, i.e. the beads-on-a-string structure with satellite droplets, the beads-on-a-string structure with no satellite droplets, the quasi-spike structure and the spike structure, are identified. At small charge levels, the perturbed jet evolves into a quasistatic beads-on-a-string structure with satellite droplets at small wavenumbers and with no satellites at large wavenumbers; at large charge levels, an unstable quasi-spike or spike structure is formed. The quasi-spike structure occurs only in the finite conductivity case, in which the non-zero tangential electrostatic force is responsible for its formation. The tangential electrostatic force also plays a role in the formation of the beads-on-a-string and the spike structures: for the former, it hinders the thinning of the filament; for the latter, it accelerates the formation of spikes at the late stages. Finite conductivity may also decrease the size of satellite droplets in the beads-on-a-string structure and leads to the transition from beads-on-a-string to quasi-spike structure. In the finite conductivity case the thinning of the filament in the beads-on-a-string structure deviates little from the $1/3De$ exponential law of non-electrified viscoelastic jets. A comparison between the finite conductivity and large conductivity cases is made. It is found that, in the large conductivity case, the axial non-uniformity of the forces, including the first normal stress difference, the capillary pressure, the electrostatic pressure and the tangential electrical force are remarkable, whereas in the finite

https://doi.org/10.1017/jfm.2019.451 Published online by Cambridge University Press

conductivity case their distributions are almost uniform in the filament. In addition, a preliminary experiment is carried out to observe spikes. The spike structure captured in the experiment is similar in appearance to that predicted by the 1-D model.

Under the slender body approximation, the flow field is simplified in the present 1-D model. On the other hand, the experimental result proves that when the deformation of the droplets gets large, the 2-D effect becomes significant, and in such a case the use of the 1-D model inevitably introduces inaccuracy. The actual 2-D motion of the liquid at large deformations is of particular interest. To test the validity of the 1-D model and to explore the 2-D nonlinear dynamics of electrically charged viscoelastic liquid jets, a robust 2-D algorithm needs to be developed.

Acknowledgements

This work was supported by the National Natural Science Foundation of China, project nos 11772328 and 11621202. We thank all the reviewers for their helpful comments and constructive suggestions.

Appendix A. The derivation of the 1-D equations

Considering symmetry, in the cylindrical coordinate system, the continuity equation is

$$\frac{1}{r}\frac{\partial}{\partial r}(rv)+\frac{\partial u}{\partial z}=0, \tag{A 1}$$

the momentum equation in the radial direction is

$$\rho\left(\frac{\partial v}{\partial t}+v\frac{\partial v}{\partial r}+u\frac{\partial v}{\partial z}\right) = -\frac{\partial p}{\partial r}+\eta_s\left(\frac{\partial^2 v}{\partial r^2}+\frac{1}{r}\frac{\partial v}{\partial r}-\frac{v}{r^2}+\frac{\partial^2 v}{\partial z^2}\right) +\frac{\partial \tau_{rr}}{\partial r}+\frac{\partial \tau_{rz}}{\partial z}+\frac{\tau_{rr}-\tau_{\theta\theta}}{r}, \tag{A 2}$$

where τ_{rz} and $\tau_{\theta\theta}$ are the $rz-$ and $\theta\theta-$ components of the polymeric stress tensor $\boldsymbol{\tau}_p$, respectively, and in the axial direction is

$$\rho\left(\frac{\partial u}{\partial t}+v\frac{\partial u}{\partial r}+u\frac{\partial u}{\partial z}\right) = -\frac{\partial p}{\partial z}+\eta_s\left(\frac{\partial^2 u}{\partial r^2}+\frac{1}{r}\frac{\partial u}{\partial r}+\frac{\partial^2 u}{\partial z^2}\right) +\frac{\partial \tau_{rz}}{\partial r}+\frac{\tau_{rz}}{r}+\frac{\partial \tau_{zz}}{\partial z}, \tag{A 3}$$

and the constitutive equations for the polymeric stress components τ_{rr}, $\tau_{\theta\theta}$, τ_{zz} and τ_{rz} are

$$\tau_{rr}+\lambda_1\left(\frac{\partial \tau_{rr}}{\partial t}+v\frac{\partial \tau_{rr}}{\partial r}+u\frac{\partial \tau_{rr}}{\partial z}-2\tau_{rr}\frac{\partial v}{\partial r}-2\tau_{rz}\frac{\partial v}{\partial z}\right)=2\eta_p\frac{\partial v}{\partial r}, \tag{A 4}$$

$$\tau_{\theta\theta}+\lambda_1\left(\frac{\partial \tau_{\theta\theta}}{\partial t}+v\frac{\partial \tau_{\theta\theta}}{\partial r}+u\frac{\partial \tau_{\theta\theta}}{\partial z}-\frac{2v}{r}\tau_{\theta\theta}\right)=2\eta_p\frac{v}{r}, \tag{A 5}$$

$$\tau_{zz}+\lambda_1\left(\frac{\partial \tau_{zz}}{\partial t}+v\frac{\partial \tau_{zz}}{\partial r}+u\frac{\partial \tau_{zz}}{\partial z}-2\tau_{rz}\frac{\partial u}{\partial r}-2\tau_{zz}\frac{\partial u}{\partial z}\right)=2\eta_p\frac{\partial u}{\partial z}, \tag{A 6}$$

https://doi.org/10.1017/jfm.2019.451 Published online by Cambridge University Press

$$\tau_{rz}+\lambda_1\left(\frac{\partial\tau_{rz}}{\partial t}+v\frac{\partial\tau_{rz}}{\partial r}+u\frac{\partial\tau_{rz}}{\partial z}+\frac{\tau_{rz}v}{r}-\tau_{rr}\frac{\partial u}{\partial r}-\tau_{zz}\frac{\partial v}{\partial z}\right)=\eta_p\left(\frac{\partial v}{\partial z}+\frac{\partial u}{\partial r}\right). \quad (A\,7)$$

The kinematic boundary condition at the jet surface $r=h(z,t)$ is

$$v=\frac{\partial h}{\partial t}+u\frac{\partial h}{\partial z}, \quad (A\,8)$$

and the normal and tangential dynamic boundary conditions are

$$p = -\frac{1}{2}\left[\varepsilon_a(E_{an}^2-E_t^2)-\varepsilon(E_n^2-E_t^2)\right]+\sigma\boldsymbol{\nabla}\cdot\boldsymbol{n}+\frac{1}{1+\left(\dfrac{\partial h}{\partial z}\right)^2}$$
$$\times\left[2\eta_s\frac{\partial v}{\partial r}+\tau_{rr}+\left(\frac{\partial h}{\partial z}\right)^2\left(2\eta_s\frac{\partial u}{\partial z}+\tau_{zz}\right)-2\frac{\partial h}{\partial z}\left(\eta_s\left(\frac{\partial v}{\partial z}+\frac{\partial u}{\partial r}\right)+\tau_{rz}\right)\right], \quad (A\,9)$$

and

$$-E_t q\left[1+\left(\frac{\partial h}{\partial z}\right)^2\right]+\left[\eta_s\left(\frac{\partial v}{\partial z}+\frac{\partial u}{\partial r}\right)+\tau_{rz}\right]\left[1-\left(\frac{\partial h}{\partial z}\right)^2\right]$$
$$+\frac{\partial h}{\partial z}\left(2\eta_s\frac{\partial v}{\partial r}+\tau_{rr}-2\eta_s\frac{\partial u}{\partial z}-\tau_{zz}\right)=0, \quad (A\,10)$$

respectively.

An alternative form of the surface charge conservation equation is

$$\frac{\partial q}{\partial t}+\boldsymbol{v}\cdot\nabla_s q-q\boldsymbol{n}\cdot(\boldsymbol{n}\cdot\boldsymbol{\nabla})\boldsymbol{v}-KE_n=0. \quad (A\,11)$$

Let ℓ_r be the typical thickness and ℓ_z be the typical axial length of the perturbed liquid jet. When the jet is a slender body, ℓ_r is much smaller than ℓ_z, that is,

$$\ell_r=\epsilon\ell_z, \quad (A\,12)$$

where ϵ is a small parameter. Let ϑ be the typical time scale. In this problem, the balance of inertia, surface tension, viscoelastic and electrostatic forces indicates that (Eggers & Villermaux 2008)

$$\eta_0\approx\rho\ell_z^2/\vartheta,\quad \sigma\approx\rho\ell_r\ell_z^2/\vartheta^2,\quad \lambda_1\approx\vartheta,\quad Q_0^2/\varepsilon_a\approx\ell_z^2/\vartheta^2, \quad (A\,13a\text{–}d)$$

and

$$\ell_z\approx\epsilon\ell_v,\quad \ell_r\approx\epsilon^2\ell_v,\quad \vartheta\approx\epsilon^2 t_v, \quad (A\,14a\text{–}c)$$

where $\ell_v=\eta_0^2/\rho\sigma$ and $t_v=\eta_0^3/\rho\sigma^2$.

Using ℓ_r, ℓ_z and ϑ to non-dimensionalize the quantities, gives

$$\left.\begin{array}{c} r=\ell_r\tilde{r},\quad z=\ell_z\tilde{z},\quad t=\vartheta\tilde{t},\quad h=\ell_r\tilde{h},\quad v=\frac{\ell_r}{\vartheta}\tilde{v},\quad u=\frac{\ell_z}{\vartheta}\tilde{u},\\ p=\frac{\rho\ell_z^2}{\vartheta^2}\tilde{p},\quad \tau_{rr}=\frac{\rho\ell_z^2}{\vartheta^2}\tilde{\tau}_{rr},\quad \tau_{\theta\theta}=\frac{\rho\ell_z^2}{\vartheta^2}\tilde{\tau}_{\theta\theta},\quad \tau_{zz}=\frac{\rho\ell_z^2}{\vartheta^2}\tilde{\tau}_{zz},\quad \tau_{rz}=\frac{\rho\ell_z^3}{\vartheta^2\ell_r}\tilde{\tau}_{rz},\end{array}\right\} \quad (A\,15)$$

https://doi.org/10.1017/jfm.2019.451 Published online by Cambridge University Press

where the tilde denotes the corresponding non-dimensional quantities. In addition, the quantities related to the electric field are non-dimensionalized by Q_0 and ε_a, i.e.

$$E_{an} = \frac{Q_0}{\varepsilon_a}\tilde{E}_{an}, \quad E_n = \frac{Q_0}{\varepsilon_a}\tilde{E}_n, \quad E_t = \frac{Q_0}{\varepsilon_a}\frac{\ell_r}{\ell_z}\tilde{E}_t, \quad q = Q_0\tilde{q}. \tag{A 16a–d}$$

Hence the non-dimensionalized governing equations are expressed as

$$\frac{\partial \tilde{v}}{\partial \tilde{r}} + \frac{\tilde{v}}{\tilde{r}} + \frac{\partial \tilde{u}}{\partial \tilde{z}} = 0, \tag{A 17}$$

$$\begin{aligned}\frac{\partial \tilde{v}}{\partial \tilde{t}} + \tilde{v}\frac{\partial \tilde{v}}{\partial \tilde{r}} + \tilde{u}\frac{\partial \tilde{v}}{\partial \tilde{z}} &= -\frac{1}{\epsilon^2}\frac{\partial \tilde{p}}{\partial \tilde{r}} + \beta\frac{1}{\epsilon^2}\left(\frac{\partial^2 \tilde{v}}{\partial \tilde{r}^2} + \frac{1}{\tilde{r}}\frac{\partial \tilde{v}}{\partial \tilde{r}} - \frac{\tilde{v}}{\tilde{r}^2}\right) + \beta\frac{\partial^2 \tilde{v}}{\partial \tilde{z}^2} \\ &\quad + \frac{1}{\epsilon^2}\frac{\partial \tilde{\tau}_{rr}}{\partial \tilde{r}} + \frac{1}{\epsilon^2}\frac{\partial \tilde{\tau}_{rz}}{\partial \tilde{z}} + \frac{1}{\epsilon^2}\frac{\tilde{\tau}_{rr} - \tilde{\tau}_{\theta\theta}}{\tilde{r}},\end{aligned} \tag{A 18}$$

$$\begin{aligned}\frac{\partial \tilde{u}}{\partial \tilde{t}} + \tilde{v}\frac{\partial \tilde{u}}{\partial \tilde{r}} + \tilde{u}\frac{\partial \tilde{u}}{\partial \tilde{z}} &= -\frac{\partial \tilde{p}}{\partial \tilde{z}} + \beta\frac{1}{\epsilon^2}\left(\frac{\partial^2 \tilde{u}}{\partial \tilde{r}^2} + \frac{1}{\tilde{r}}\frac{\partial \tilde{u}}{\partial \tilde{r}}\right) + \beta\frac{\partial^2 \tilde{u}}{\partial \tilde{z}^2} \\ &\quad + \frac{1}{\epsilon^2}\frac{\partial \tilde{\tau}_{rz}}{\partial \tilde{r}} + \frac{1}{\epsilon^2}\frac{\tilde{\tau}_{rz}}{\tilde{r}} + \frac{\partial \tilde{\tau}_{zz}}{\partial \tilde{z}},\end{aligned} \tag{A 19}$$

$$\tilde{\tau}_{rr} + \frac{\partial \tilde{\tau}_{rr}}{\partial \tilde{t}} + \tilde{v}\frac{\partial \tilde{\tau}_{rr}}{\partial \tilde{r}} + \tilde{u}\frac{\partial \tilde{\tau}_{rr}}{\partial \tilde{z}} - 2\tilde{\tau}_{rr}\frac{\partial \tilde{v}}{\partial \tilde{r}} - 2\tilde{\tau}_{rz}\frac{\partial \tilde{v}}{\partial \tilde{z}} = 2(1-\beta)\frac{\partial \tilde{v}}{\partial \tilde{r}}, \tag{A 20}$$

$$\tilde{\tau}_{\theta\theta} + \frac{\partial \tilde{\tau}_{\theta\theta}}{\partial \tilde{t}} + \tilde{v}\frac{\partial \tilde{\tau}_{\theta\theta}}{\partial \tilde{r}} + \tilde{u}\frac{\partial \tilde{\tau}_{\theta\theta}}{\partial \tilde{z}} - \frac{2\tilde{v}}{\tilde{r}}\tilde{\tau}_{\theta\theta} = 2(1-\beta)\frac{\tilde{v}}{\tilde{r}}, \tag{A 21}$$

$$\tilde{\tau}_{zz} + \frac{\partial \tilde{\tau}_{zz}}{\partial \tilde{t}} + \tilde{v}\frac{\partial \tilde{\tau}_{zz}}{\partial \tilde{r}} + \tilde{u}\frac{\partial \tilde{\tau}_{zz}}{\partial \tilde{z}} - 2\frac{1}{\epsilon^2}\tilde{\tau}_{rz}\frac{\partial \tilde{u}}{\partial \tilde{r}} - 2\tilde{\tau}_{zz}\frac{\partial \tilde{u}}{\partial \tilde{z}} = 2(1-\beta)\frac{\partial \tilde{u}}{\partial \tilde{z}}, \tag{A 22}$$

$$\tilde{\tau}_{rz} + \frac{\partial \tilde{\tau}_{rz}}{\partial \tilde{t}} + \tilde{v}\frac{\partial \tilde{\tau}_{rz}}{\partial \tilde{r}} + \tilde{u}\frac{\partial \tilde{\tau}_{rz}}{\partial \tilde{z}} + \frac{\tilde{\tau}_{rz}\tilde{v}}{\tilde{r}} - \tilde{\tau}_{rr}\frac{\partial \tilde{u}}{\partial \tilde{r}} - \epsilon^2\tilde{\tau}_{zz}\frac{\partial \tilde{v}}{\partial \tilde{z}} = (1-\beta)\left(\epsilon^2\frac{\partial \tilde{v}}{\partial \tilde{z}} + \frac{\partial \tilde{u}}{\partial \tilde{r}}\right), \tag{A 23}$$

and the non-dimensionalized boundary conditions at the jet surface $\tilde{r} = \tilde{h}(\tilde{z}, \tilde{t})$ are

$$\tilde{v} = \frac{\partial \tilde{h}}{\partial \tilde{t}} + \tilde{u}\frac{\partial \tilde{h}}{\partial \tilde{z}}, \tag{A 24}$$

$$\begin{aligned}\tilde{p} &= -\frac{1}{2}\left[\left(\tilde{E}_{an}^2 - \tilde{E}_t^2\right) - \varepsilon_r\left(\tilde{E}_n^2 - \tilde{E}_t^2\right)\right] + \tilde{\boldsymbol{\nabla}}\cdot\tilde{\boldsymbol{n}} + \frac{1}{1+\epsilon^2\left(\dfrac{\partial \tilde{h}}{\partial \tilde{z}}\right)^2} \\ &\quad \times\left[2\beta\frac{\partial \tilde{v}}{\partial \tilde{r}} + \tilde{\tau}_{rr} + \epsilon^2\left(\frac{\partial \tilde{h}}{\partial \tilde{z}}\right)^2\left(2\beta\frac{\partial \tilde{u}}{\partial \tilde{z}} + \tilde{\tau}_{zz}\right) - 2\frac{\partial \tilde{h}}{\partial \tilde{z}}\left(\beta\left(\epsilon^2\frac{\partial \tilde{v}}{\partial \tilde{z}} + \frac{\partial \tilde{u}}{\partial \tilde{r}}\right) + \tilde{\tau}_{rz}\right)\right],\end{aligned} \tag{A 25}$$

$$-\tilde{E}_t\tilde{q}\left[1+\epsilon^2\left(\frac{\partial \tilde{h}}{\partial \tilde{z}}\right)^2\right] + \left[\beta\left(\frac{\partial \tilde{v}}{\partial \tilde{z}} + \frac{1}{\epsilon^2}\frac{\partial \tilde{u}}{\partial \tilde{r}}\right) + \frac{1}{\epsilon^2}\tilde{\tau}_{rz}\right]\left[1-\epsilon^2\left(\frac{\partial \tilde{h}}{\partial \tilde{z}}\right)^2\right]$$

https://doi.org/10.1017/jfm.2019.451 Published online by Cambridge University Press

$$+\frac{\partial \tilde{h}}{\partial \tilde{z}}\left[2\beta\frac{\partial \tilde{v}}{\partial \tilde{r}}+\tilde{\tau}_{rr}-2\beta\frac{\partial \tilde{u}}{\partial \tilde{z}}-\tilde{\tau}_{zz}\right]=0, \tag{A 26}$$

$$\frac{\partial \tilde{q}}{\partial \tilde{t}}+\tilde{\boldsymbol{v}}\cdot\tilde{\nabla}_s\tilde{q}-\tilde{q}\tilde{\boldsymbol{n}}\cdot(\tilde{\boldsymbol{n}}\cdot\tilde{\nabla})\tilde{\boldsymbol{v}}-\tau\varepsilon_r\tilde{E}_n=0. \tag{A 27}$$

Under the slender body approximation, the quantities can be expanded into a Taylor series of the radial coordinate $\epsilon\tilde{r}$ as follows (Chang *et al.* 1999; López-Herrera *et al.* 1999; Eggers & Villermaux 2008),

$$\tilde{u} = \tilde{u}_0(\tilde{z},\tilde{t})+\tilde{u}_2(\tilde{z},\tilde{t})\frac{(\epsilon\tilde{r})^2}{2}+\cdots, \tag{A 28}$$

$$\epsilon\tilde{v} = -\frac{\partial \tilde{u}_0}{\partial \tilde{z}}(\tilde{z},\tilde{t})\frac{\epsilon\tilde{r}}{2}-\frac{\partial \tilde{u}_2}{\partial \tilde{z}}(\tilde{z},\tilde{t})\frac{(\epsilon\tilde{r})^3}{8}+\cdots, \tag{A 29}$$

$$\tilde{p} = \tilde{p}_0(\tilde{z},\tilde{t})+\tilde{p}_2(\tilde{z},\tilde{t})(\epsilon\tilde{r})^2+\cdots, \tag{A 30}$$

$$\tilde{\tau}_{rr} = \tilde{\tau}_{rr0}(\tilde{z},\tilde{t})+\tilde{\tau}_{rr2}(\tilde{z},\tilde{t})(\epsilon\tilde{r})^2+\cdots, \tag{A 31}$$

$$\tilde{\tau}_{\theta\theta} = \tilde{\tau}_{\theta\theta0}(\tilde{z},\tilde{t})+\tilde{\tau}_{\theta\theta2}(\tilde{z},\tilde{t})(\epsilon\tilde{r})^2+\cdots, \tag{A 32}$$

$$\tilde{\tau}_{zz} = \tilde{\tau}_{zz0}(\tilde{z},\tilde{t})+\tilde{\tau}_{zz2}(\tilde{z},\tilde{t})(\epsilon\tilde{r})^2+\cdots, \tag{A 33}$$

$$\tilde{r}\tilde{\tau}_{rz} = \tilde{\tau}_{rz0}(\tilde{z},\tilde{t})+\tilde{\tau}_{rz2}(\tilde{z},\tilde{t})(\epsilon\tilde{r})^2+\cdots. \tag{A 34}$$

The above expansions of the velocity components $\tilde{u}$ and $\tilde{v}$ automatically satisfy the continuity equation (A 17). Substituting the expansions (A 28)–(A 34) into (A 18)–(A 27) and keeping only those leading-order terms yields

$$\tilde{\tau}_{rr0}=\tilde{\tau}_{\theta\theta0},\quad \tilde{\tau}_{rz0}=0, \tag{A 35}$$

$$\frac{\partial \tilde{u}_0}{\partial \tilde{t}}+\tilde{u}_0\frac{\partial \tilde{u}_0}{\partial \tilde{z}}=-\frac{\partial \tilde{p}_0}{\partial \tilde{z}}+\beta\left(2\tilde{u}_2+\frac{\partial^2\tilde{u}_0}{\partial \tilde{z}^2}\right)+2\tilde{\tau}_{rz2}+\frac{\partial \tilde{\tau}_{zz0}}{\partial \tilde{z}}, \tag{A 36}$$

$$\tilde{\tau}_{rr0}+\frac{\partial \tilde{\tau}_{rr0}}{\partial \tilde{t}}+\tilde{u}_0\frac{\partial \tilde{\tau}_{rr0}}{\partial \tilde{z}}+\tilde{\tau}_{rr0}\frac{\partial \tilde{u}_0}{\partial \tilde{z}}=-(1-\beta)\frac{\partial \tilde{u}_0}{\partial \tilde{z}}, \tag{A 37}$$

$$\tilde{\tau}_{\theta\theta0}+\frac{\partial \tilde{\tau}_{\theta\theta0}}{\partial \tilde{t}}+\tilde{u}_0\frac{\partial \tilde{\tau}_{\theta\theta0}}{\partial \tilde{z}}+\tilde{\tau}_{\theta\theta0}\frac{\partial \tilde{u}_0}{\partial \tilde{z}}=-(1-\beta)\frac{\partial \tilde{u}_0}{\partial \tilde{z}}, \tag{A 38}$$

$$\tilde{\tau}_{zz0}+\frac{\partial \tilde{\tau}_{zz0}}{\partial \tilde{t}}+\tilde{u}_0\frac{\partial \tilde{\tau}_{zz0}}{\partial \tilde{z}}-2\tilde{\tau}_{zz0}\frac{\partial \tilde{u}_0}{\partial \tilde{z}}=2(1-\beta)\frac{\partial \tilde{u}_0}{\partial \tilde{z}}, \tag{A 39}$$

$$\tilde{\tau}_{rz2}+\frac{\partial \tilde{\tau}_{rz2}}{\partial \tilde{t}}-\tilde{\tau}_{rz2}\frac{\partial \tilde{u}_0}{\partial \tilde{z}}+\tilde{u}_0\frac{\partial \tilde{\tau}_{rz2}}{\partial \tilde{z}}-\tilde{\tau}_{rr0}\tilde{u}_2+\frac{1}{2}\tilde{\tau}_{zz0}\frac{\partial^2\tilde{u}_0}{\partial \tilde{z}^2}$$
$$=(1-\beta)\left(\tilde{u}_2-\frac{1}{2}\frac{\partial^2\tilde{u}_0}{\partial \tilde{z}^2}\right), \tag{A 40}$$

$$\frac{\partial \tilde{h}}{\partial \tilde{t}}+\tilde{u}_0\frac{\partial \tilde{h}}{\partial \tilde{z}}=-\frac{\tilde{h}}{2}\frac{\partial \tilde{u}_0}{\partial \tilde{z}}, \tag{A 41}$$

$$\tilde{p}_0=-\frac{1}{2}\left[(\tilde{E}_{an}^2-\tilde{E}_t^2)-\varepsilon_r(\tilde{E}_n^2-\tilde{E}_t^2)\right]+\tilde{\nabla}\cdot\tilde{\boldsymbol{n}}-\beta\frac{\partial \tilde{u}_0}{\partial \tilde{z}}+\tilde{\tau}_{rr0}, \tag{A 42}$$

$$\tilde{\nabla}\cdot\tilde{\boldsymbol{n}}=\frac{1}{\left[1+\epsilon^2\left(\dfrac{\partial \tilde{h}}{\partial \tilde{z}}\right)^2\right]^{3/2}}\left[\frac{1+\epsilon^2\left(\dfrac{\partial \tilde{h}}{\partial \tilde{z}}\right)^2}{\tilde{h}}-\epsilon^2\frac{\partial^2\tilde{h}}{\partial \tilde{z}^2}\right], \tag{A 43}$$

https://doi.org/10.1017/jfm.2019.451 Published online by Cambridge University Press

$$\beta\tilde{u}_2+\tilde{\tau}_{rz2}=\frac{1}{2}\beta\frac{\partial^2\tilde{u}_0}{\partial\tilde{z}^2}+\frac{1}{\tilde{h}}\frac{\partial\tilde{h}}{\partial\tilde{z}}\left(3\beta\frac{\partial\tilde{u}_0}{\partial\tilde{z}}-\tilde{\tau}_{rr0}+\tilde{\tau}_{zz0}\right)+\frac{\tilde{E}_t\tilde{q}}{\tilde{h}}\left[1+\epsilon^2\left(\frac{\partial\tilde{h}}{\partial\tilde{z}}\right)^2\right], \tag{A 44}$$

$$\frac{\partial\tilde{q}}{\partial\tilde{t}}+\tilde{u}_0\frac{\partial\tilde{q}}{\partial\tilde{z}}+\frac{\tilde{q}}{2}\frac{\partial\tilde{u}_0}{\partial\tilde{z}}-\tau\varepsilon_r\tilde{E}_n=0. \tag{A 45}$$

Substituting the tangential dynamic boundary condition (A 44) into the $z-$ momentum equation (A 36) to replace the terms related to $\tilde{u}_2$ and $\tilde{\tau}_{rz2}$ yields

$$\begin{aligned}\frac{\partial\tilde{u}_0}{\partial\tilde{t}}+\tilde{u}_0\frac{\partial\tilde{u}_0}{\partial\tilde{z}} &= -\frac{\partial\tilde{p}_0}{\partial\tilde{z}}+\beta\left(2\frac{\partial^2\tilde{u}_0}{\partial\tilde{z}^2}+\frac{6}{\tilde{h}}\frac{\partial\tilde{h}}{\partial\tilde{z}}\frac{\partial\tilde{u}_0}{\partial\tilde{z}}\right)+\frac{2}{\tilde{h}}\frac{\partial\tilde{h}}{\partial\tilde{z}}(\tilde{\tau}_{zz0}-\tilde{\tau}_{rr0})\\ &\quad+\frac{\partial\tilde{\tau}_{zz0}}{\partial\tilde{z}}+\frac{2\tilde{E}_t\tilde{q}}{\tilde{h}}\left[1+\epsilon^2\left(\frac{\partial\tilde{h}}{\partial\tilde{z}}\right)^2\right].\end{aligned} \tag{A 46}$$

Differentiating the normal dynamic boundary condition (A 42) with respect to $\tilde{z}$ yields

$$\frac{\partial\tilde{p}_0}{\partial\tilde{z}}=-\frac{1}{2}\frac{\partial}{\partial\tilde{z}}\left[(\tilde{E}_{an}^2-\tilde{E}_t^2)-\varepsilon_r\left(\tilde{E}_n^2-\tilde{E}_t^2\right)\right]+\frac{\partial}{\partial\tilde{z}}(\tilde{\boldsymbol{\nabla}}\cdot\tilde{\boldsymbol{n}})-\beta\frac{\partial^2\tilde{u}_0}{\partial\tilde{z}^2}+\frac{\partial\tilde{\tau}_{rr0}}{\partial\tilde{z}}. \tag{A 47}$$

Finally, substituting (A 47) into (A 46) to replace the pressure gradient there, one gets

$$\begin{aligned}\frac{\partial\tilde{u}_0}{\partial\tilde{t}}+\tilde{u}_0\frac{\partial\tilde{u}_0}{\partial\tilde{z}} &= \frac{1}{2}\frac{\partial}{\partial\tilde{z}}\left[(\tilde{E}_{an}^2-\tilde{E}_t^2)-\varepsilon_r(\tilde{E}_n^2-\tilde{E}_t^2)\right]+\frac{2\tilde{E}_t\tilde{q}}{\tilde{h}}\left[1+\epsilon^2\left(\frac{\partial\tilde{h}}{\partial\tilde{z}}\right)^2\right]\\ &\quad-\frac{\partial}{\partial\tilde{z}}\left(\tilde{\boldsymbol{\nabla}}\cdot\tilde{\boldsymbol{n}}\right)+3\beta\frac{1}{\tilde{h}^2}\frac{\partial}{\partial\tilde{z}}\left(\tilde{h}^2\frac{\partial\tilde{u}_0}{\partial\tilde{z}}\right)+\frac{1}{\tilde{h}^2}\frac{\partial}{\partial\tilde{z}}\left[\tilde{h}^2(\tilde{\tau}_{zz0}-\tilde{\tau}_{rr0})\right].\end{aligned} \tag{A 48}$$

The equations (A 41), (A 48), (A 43), (A 37), (A 39) and (A 45) constitute our 1-D system. It should be emphasized that in this 1-D system the full expression of the curvature is retained and the electric field is not simplified under the slender body approximation. As other researchers suggested (Ambravaneswaran *et al.* 2002; Li & Fontelos 2003; Clasen *et al.* 2006; Collins *et al.* 2007; Eggers & Villermaux 2008), this strategy may ensure the accuracy of the 1-D simulation to a great extent when the deformation of the jet is large.

The 1-D equations restored to their dimensional form are written as

$$\frac{\partial h}{\partial t}+u\frac{\partial h}{\partial z}=-\frac{h}{2}\frac{\partial u}{\partial z}, \tag{A 49}$$

$$\begin{aligned}\rho\left(\frac{\partial u}{\partial t}+u\frac{\partial u}{\partial z}\right) &= \frac{1}{2}\frac{\partial}{\partial z}\left[\varepsilon_a(E_{an}^2-E_t^2)-\varepsilon\left(E_n^2-E_t^2\right)\right]+\frac{2E_tq}{h}\left[1+\left(\frac{\partial h}{\partial z}\right)^2\right]\\ &\quad-\sigma\frac{\partial(\boldsymbol{\nabla}\cdot\boldsymbol{n})}{\partial z}+3\eta_s\frac{1}{h^2}\frac{\partial}{\partial z}\left(h^2\frac{\partial u}{\partial z}\right)+\frac{1}{h^2}\frac{\partial}{\partial z}\left[h^2(\tau_{zz}-\tau_{rr})\right],\end{aligned} \tag{A 50}$$

https://doi.org/10.1017/jfm.2019.451 Published online by Cambridge University Press

$$\nabla \cdot \boldsymbol{n} = \frac{1}{\left[1+\left(\dfrac{\partial h}{\partial z}\right)^2\right]^{3/2}}\left[\frac{1+\left(\dfrac{\partial h}{\partial z}\right)^2}{h} - \frac{\partial^2 h}{\partial z^2}\right], \tag{A 51}$$

$$\tau_{zz} + \lambda_1\left(\frac{\partial \tau_{zz}}{\partial t} + u\frac{\partial \tau_{zz}}{\partial z} - 2\tau_{zz}\frac{\partial u}{\partial z}\right) = 2\eta_p\frac{\partial u}{\partial z}, \tag{A 52}$$

$$\tau_{rr} + \lambda_1\left(\frac{\partial \tau_{rr}}{\partial t} + u\frac{\partial \tau_{rr}}{\partial z} + \tau_{rr}\frac{\partial u}{\partial z}\right) = -\eta_p\frac{\partial u}{\partial z}, \tag{A 53}$$

$$\frac{\partial q}{\partial t} + u\frac{\partial q}{\partial z} + \frac{q}{2}\frac{\partial u}{\partial z} - KE_n = 0, \tag{A 54}$$

where the subscript 0 is dropped for brevity. Now using the radius of the jet R, the capillary time $t_c = \sqrt{\rho R^3/\sigma}$, the capillary force σ/R, the zero-shear viscosity η_0, the electric field strength Q_0/ε_a and the electrical permittivity of the air ε_a as scales to non-dimensionalize (A 49)–(A 54), one obtains the 1-D equations (2.14)–(2.19) in non-dimensional form.

REFERENCES

ALSHARIF, A. M., UDDIN, J. & AFZAAL, M. F. 2015 Instability of viscoelastic curved liquid jets. *Appl. Math. Model.* **39**, 3924–3938.

AMBRAVANESWARAN, B., WILKES, E. D. & BASARAN, O. A. 2002 Drop formation from a capillary cube: comparison of one-dimensional and two-dimensional analyses and occurrence of satellite drops. *Phys. Fluids* **14**, 2606–2621.

ANNA, S. L. & MCKINLEY, G. H. 2001 Elasto-capillary thinning and breakup of model elastic liquids. *J. Rheol.* **45**, 115–138.

ARDEKANI, A. M., SHARMA, V. & MCKINLEY, G. H. 2010 Dynamics of bead formation, filament thinning and breakup in weakly viscoelastic jets. *J. Fluid Mech.* **665**, 46–56.

BASARAN, O. A., GAO, H. & BHAT, P. P. 2013 Nonstandard inkjets. *Annu. Rev. Fluid Mech.* **45**, 85–113.

BAZILEVSKII, A. V. & ROZHKOV, A. N. 2014 Dynamics of capillary breakup of elastic jets. *Fluid Dyn.* **49**, 827–843.

BHAT, P. P., APPATHURAI, S., HARRIS, M. T. & BASARAN, O. A. 2012 On self-similarity in the drop-filament corner region formed during pinch-off of viscoelastic fluid threads. *Phys. Fluids* **24**, 083101.

BHAT, P. P., APPATHURAI, S., HARRIS, M. T., PASQUALI, M., MCKINLEY, G. H. & BASARAN, O. A. 2010 Formation of beads-on-a-string structures during break-up of viscoelastic filaments. *Nat. Phys.* **6**, 625–631.

BOUSFIELD, D. W., KEUNINGS, R., MARRUCCI, G. & DENN, M. M. 1986 Nonlinear analysis of the surface tension driven breakup of viscoelastic filaments. *J. Non-Newtonian Fluid Mech.* **1986**, 79–97.

BRENN, G. & TEICHTMEISTER, S. 2013 Linear shape oscillations and polymeric time scales of viscoelastic drops. *J. Fluid Mech.* **733**, 504–527.

CHANG, H.-C., DEMEKHIN, E. A. & KALAIDIN, E. 1999 Iterated stretching of viscoelastic jets. *Phys. Fluids* **11**, 1717–1737.

CHRISTANTI, Y. & WALKER, L. M. 2001 Surface tension driven jet break up of strain-hardening polymer solutions. *J. Non-Newtonian Fluid Mech.* **100**, 9–26.

CHRISTANTI, Y. & WALKER, L. M. 2002 Effect of fluid relaxation time of dilute polymer solutions on jet breakup due to a forced disturbance. *J. Rheol.* **46**, 733–748.

https://doi.org/10.1017/jfm.2019.451 Published online by Cambridge University Press

CLASEN, C., BICO, J., ENTOV, V. M. & MCKINLEY, G. H. 2009 'Gobbling drops': the jetting-dripping transition in flows of polymer solutions. *J. Fluid Mech.* **636**, 5–40.

CLASEN, C., EGGERS, J., FONTELOS, M. A., LI, J. & MCKINLEY, G. H. 2006 The beads-on-string structure of viscoelastic threads. *J. Fluid Mech.* **556**, 283–308.

COLLINS, R. T., HARRIS, M. T. & BASARAN, O. A. 2007 Breakup of electrified jets. *J. Fluid Mech.* **588**, 75–129.

DEBLAIS, A., VELIKOV, K. P. & BONN, D. 2018 Pearling instabilities of a viscoelastic thread. *Phys. Rev. Lett.* **120**, 194501.

EDA, G. & SHIVKUMAR, S. 2007 Bead-to-fiber transition in electrospun polystyrene. *J. Appl. Polym. Sci.* **106**, 475–487.

EGGERS, J. 2014 Instability of a polymeric thread. *Phys. Fluids* **26**, 033106.

EGGERS, J. & VILLERMAUX, E. 2008 Physics of liquid jets. *Rep. Prog. Phys.* **71**, 036601.

ELCOOT, A. E. K. 2007 Nonlinear instability of charged liquid jets: effect of interfacial charge relaxation. *Phys.* A **375**, 411–428.

ENTOV, V. M. & HINCH, E. J. 1997 Effect of a spectrum of relaxation times on the capillary thinning of a filament of elastic liquid. *J. Non-Newtonian Fluid Mech.* **72**, 31–53.

FENG, J. J. 2003 Streching of a straight electrically charged viscoelastic jet. *J. Non-Newtonian Fluid Mech.* **116**, 55–70.

FONTELOS, M. A. & LI, J. 2004 On the evolution and rupture of filaments in Giesekus and FENE models. *J. Non-Newtonian Fluid Mech.* **118**, 1–16.

GAÑÁN-CALVO, A. M., LÓPEZ-HERRERE, J. M., HERRADA, M. A., RAMOS, A. & MONTANERO, J. M. 2018 Review on the physics of electrospray: from electrokinetics to the operating conditions of single and coaxial Taylor cone-jets, and AC electrospray. *J. Aero. Sci.* **125**, 32–56.

GREICIUNAS, E., WONG, J., GORBATENKO, I., HALL, J., WILSON, M. C. T., KAPUR, N., HARLEN, O. G., VADILLO, D. & THRELFALL-HOLMES, P. 2017 Design and operation of a Rayleigh Ohnesorge jetting extensinoal rheometer (ROJER) to study extensional properties of low viscosity polymer solutions. *J. Rheol.* **61**, 467–476.

GUPTA, K. & CHOKSHI, P. 2015 Weakly nonlinear stability analysis of polymer fibre spinning. *J. Fluid Mech.* **776**, 268–289.

HIGUERA, F. J. 2003 Flow rate and electric current emitted by a Taylor cone. *J. Fluid Mech.* **484**, 303–327.

HIGUERA, F. J. 2006 Stationary viscosity-dominated electrified capillary jets. *J. Fluid Mech.* **558**, 143–152.

ISMAIL, N., MAKSOUD, F. J., GHADDAR, N., GHALI, K. & TEHRANI-BAGHA, A. 2016 Simplified modeling of the electrospinning process from the stable jet region to the unstable region for predicting the final nanofiber diameter. *J. Appl. Polym. Sci.* **133**, 44112.

JAMES, D. F. 2009 Boger fluids. *Annu. Rev. Fluid Mech.* **41**, 129–142.

JIMENEZ, L. N., DINIC, J., PARSI, N. & SHARMA, V. 2018 Extensional relaxation time, pinch-off dynamics, and printability of semidilute polyelectrolyte solutions. *Macromolecules* **51**, 5191–5208.

KHISMATULLIN, D. B. & NADIM, A. 2001 Shape oscillations of a viscoelastic drop. *Phys. Rev.* E **63**, 061508.

KULICHIKHIN, V. G., MALKIN, A. Y., SEMAKOV, A. V., SKVORTSOV, I. Y. & ARINSTEIN, A. 2014 Liquid filament instability due to stretch-induced phase separation in polymer solutions. *Eur. Phys. J. E.* **37**, 10.

LAKDAWALA, A. M., SHARMA, A. & THAOKAR, R. 2016 A dual grid level set method based study on similarity and difference bewteen interface dynamics for surface tension and radial electric field induced jet breakup. *Chem. Engng Sci.* **148**, 238–255.

LI, F., YIN, X.-Y. & YIN, X.-Z. 2011 Axisymmetric and non-axisymmetric instability of an electrically charged viscoelastic liquid jet. *J. Non-Newtonian Fluid Mech.* **166**, 1024–1032.

LI, F., YIN, X.-Y. & YIN, X.-Z. 2016 One-dimensional nonlinear instability study of a slightly viscoelastic, perfectly conducting liquid jet under a radial electric field. *Phys. Fluids* **28**, 053103.

https://doi.org/10.1017/jfm.2019.451 Published online by Cambridge University Press

LI, F., YIN, X.-Y. & YIN, X.-Z. 2017*a* Oscillation of satellite droplets in an Oldroyd-B viscoelastic liquid jet. *Phys. Rev. Fluids* **2**, 013602.

LI, F., YIN, X.-Y. & YIN, X.-Z. 2017*b* Transition from a beads-on-string to a spilke structure in an electrified viscoelastic jet. *Phys. Fluids* **29**, 023106.

LI, F., YIN, X.-Y. & YIN, X.-Z. 2019 Small-amplitude shape oscillation and linear instability of an electrically charged viscoelastic liquid droplet. *J. Non-Newtonian Fluid Mech.* **264**, 85–97.

LI, J. & FONTELOS, M. A. 2003 Drop dynamics on the beads-on-string structure for viscoelastic jets: a numerical study. *Phys. Fluids* **15**, 922–937.

LÓPEZ-HERRERA, J. M. & GAÑÁN-CALVO, A. M. 2004 A note on charged capillary jet breakup of conducting liquids: experimental validation of a viscous one-dimensional model. *J. Fluid Mech.* **501**, 303–326.

LÓPEZ-HERRERA, J. M., GAÑÁN-CALVO, A. M. & PEREZ-SABORID, M. 1999 One-dimensional simulation of the breakup of capillary jets of conducting liquids. Application to E.H.D. spraying. *J. Aero. Sci.* **30**, 895–912.

LÓPEZ-HERRERA, J. M., GAÑÁN-CALVO, A. M., POPINET, S. & HERRADA, M. A. 2015 Electrokinetic effects in the breakup of electrified jets: a volume-of-fluid numerical study. *Intl J. Multiphase Flow* **71**, 14–22.

LÓPEZ-HERRERA, J. M., RIESCO-CHUECA, P. & GAÑÁN-CALVO, A. M. 2005 Linear stability analysis of axisymmetric perturbations in imperfectly conducting liquid jets. *Phys. Fluids* **17**, 034106.

MALKIN, A. Y., ARINSTEIN, A. & KULICHIKHIN, V. G. 2014 Polymer extension flows and instabilities. *Prog. Polym. Sci.* **39**, 959–978.

MATHUES, W., FORMENTI, S., MCILROY, C., HARLEN, O. G. & CLASEN, C. 2018 CaBER vs ROJER – different time scales for the thinning of a weakly elastic jet. *J. Rheol.* **62**, 1135–1153.

MELCHER, J. R. & TAYLOR, G. I. 1969 Electrohydrodynamics: a review of the role of interfacial shear stresses. *Annu. Rev. Fluid Mech.* **1**, 111–146.

MOHAMED, A. S., HERRADA, M. A., GAÑÁN-CALVO, A. M. & MONTANERO, J. M. 2015 Convective-to-absolute instability transition in a viscoelastic capillary jet subject to unrelaxed axial elastic tension. *Phys. Rev.* E **92**, 023006.

MORRISON, N. F. & HARLEN, O. G. 2010 Viscoelasticity in inkjet printing. *Rheol. Acta* **49**, 619–632.

OLIVEIRA, M. S. N., YEH, R. & MCKINLEY, G. H. 2006 Iterated stretching, extensional rheology and formation of beads-on-a-string structures in polymer solutions. *J. Non-Newtonian Fluid Mech.* **137**, 137–148.

ONSES, M. S., SUTANTO, E., FERREIRA, P. M. & ALLEYNE, A. G. 2015 Mechanisms, capabilities, and applications of high-resolutions electrohydrodynamic jet printing. *Small* **11**, 4237–4266.

PRILUTSKI, G., GUPTA, R. K., SRIDHAR, T. & RYAN, M. E. 1983 Model viscoelastic liquids. *J. Non-Newtonian Fluid Mech.* **12**, 233–241.

RAYLEIGH, L. 1878 On the instability of jets. *Proc. Lond. Math. Soc.* **10**, 4–13.

RAYLEIGH, L. 1879 On the capillary phenomena of jets. *Proc. R. Soc. Lond.* **29**, 71–97.

ROSELL-LLOMPART, J., GRIFOLL, J. & LOSCERTALES, I. G. 2018 Electrosprays in the cone-jet mode: from Taylor cone formation to spray development. *J. Aero. Sci.* **125**, 2–31.

RUO, A.-C., CHEN, K.-H., CHANG, M.-H. & CHEN, F. 2012 Instability of a charged non-Newtonian liquid jet. *Phys. Rev.* E **85**, 016306.

SATTLER, R., GIER, S., EGGERS, J. & WAGNER, C. 2012 The final stages of capillary break-up of polymer solutions. *Phys. Fluids* **24**, 023101.

SATTLER, R., WAGNER, C. & EGGERS, J. 2008 Blistering pattern and formation of nanofibers in capillary thinning of polymer solutions. *Phys. Rev. Lett.* **100**, 164502.

SAVILLE, D. A. 1997 Electrohydrodynamics: the Taylor–Melcher leaky dielectric model. *Annu. Rev. Fluid Mech.* **29**, 27–64.

SCHÜMMER, P. & THELEN, H.-G. 1988 Break-up of a viscoelastic liquid jet. *Rheol. Acta* **27**, 39–43.

SETIAWAN, E. R. & HEISTER, S. D. 1997 Nonlinear modeling of an infinite electrified jet. *J. Electrostat.* **42**, 243–257.

TEMBELY, M., VADILLO, D., MACKLEY, M. R. & SOUCEMARIANADIN, A. 2012 The matching of a one-dimensional numerical simulation and experiment results for low viscosity Newtonian

https://doi.org/10.1017/jfm.2019.451 Published online by Cambridge University Press

and non-Newtonian fluids during fast filament stretching and subsequent break-up. *J. Rheol.* **56**, 159–183.

TIRTAATMADJA, V., MCKINLEY, G. H. & COOPER-WHITE, J. J. 2006 Drop formation and breakup of low viscosity elastic fluids: effects of molecular weight and concentration. *Phys. Fluids* **18**, 043101.

TURKOZ, E., LOPEZ-HERRERA, J. M., EGGERS, J., ARNOLD, C. B. & DEIKE, L. 2018 Axisymmetric simulation of viscoelastic filament thinning with the Oldroyd-B model. *J. Fluid Mech.* **851**, R2.

VARCHANIS, S., DIMAKOPOULOS, Y., WAGNER, C. & TSAMOPOULOS, J. 2018 How viscoelastic is human blood plasma? *Soft Matt.* **14**, 4238–4251.

WAGNER, C., AMAROUCHENE, Y., BONN, D. & EGGERS, J. 2005 Droplet detachment and satellite bead formation in viscoelastic fluids. *Phys. Rev. Lett.* **95**, 164504.

WAGNER, C., BOUROUIBA, L. & MCKINLEY, G. H. 2015 An analytic solution for capillary thinning and breakup of FENE-P fluids. *J. Non-Newtonian Fluid Mech.* **218**, 53–61.

WANG, C., WANG, Y. & HASHIMOTO, T. 2016 Impact of entanglement density on solution electrospinning: a phenomenological model for fiber diameter. *Macromolecules* **49**, 7985–7996.

WANG, Q. 2012 Breakup of a poorly conducting liquid thread subject to a radial electric field at zero Reynolds number. *Phys. Fluids* **24**, 102102.

WANG, Q., MÄHLMANN, S. & PAPAGEORGIOU, D. T. 2009 Dynamics of liquid jets and threads under the action of radial electric fields: microthread formation and touchdown singularities. *Phys. Fluids* **21**, 032109.

WANG, Q. & PAPAGEORGIOU, D. T. 2011 Dynamics of a viscous thread surrounded by another viscous fluid in a cylindrical tube under the action of radial electric fields: breakup and touchdown singularities. *J. Fluid Mech.* **683**, 27–56.

WANG, Y., HASHIMOTO, T., LI, C.-C., LI, Y.-C. & WANG, C. 2018 Extension rate of the straight jet in electrospinning of poly(*N*-isopropylacrylamide) solutions in dimethylformamide: influences of flow rate and applied voltage. *J. Polym. Sci.* B **56**, 319–329.

YANG, L. J., LIU, Y. X. & FU, Q. F. 2012 Linear stability analysis of an electrified viscoelastic liquid jet. *J. Fluids Engng* **134**, 071303.

YOON, J., YANG, H.-S., ADN, B.-S. L. & YU, W.-R. 2018 Recent progress in coaxial electrospinning: new parameters, various structures, and wide applications. *Adv. Mater.* **30**, 1704765.

YU, J. H., FRIDRIKH, S. V. & RUTLEDGE, G. C. 2006 The role of elasticity in the formation of electrospun fibers. *Polymer* **47**, 4789–4797.

ZELL, A., GIER, S., RAFAÏ, S. & WAGNER, C. 2010 Is there a relation between the relaxation time measured in CaBER experiments and the first normal stress coefficient? *J. Non-Newtonian Fluid Mech.* **165**, 1265–1274.

https://doi.org/10.1017/jfm.2019.451 Published online by Cambridge University Press